# Smooth Particle Hydrodynamics with nonlinear Moving-Least-Squares WENO reconstruction to model anisotropic dispersion in porous media

CrossMark

Diego Avesani [a,*], Paulo Herrera [b], Gabriele Chiogna [c,d], Alberto Bellin [a], Michael Dumbser [a]

[a] Department of Civil, Environmental and Mechanical Engineering, University of Trento, via Mesiano 77, I-38123 Trento, Italy
[b] Department of Civil Engineering, University of Chile, Av. Blanco Encalada 2002, Santiago 8370449, Chile
[c] Center for Applied Geoscience, University of Tübingen, Hölderlinstr. 12, 72074 Tübingen, Germany
[d] Faculty for Civil, Geo and Environmental Engineering, Technical University of Munich, Darcistrasse 21, 80333 Munich, Germany

## ARTICLE INFO

## ABSTRACT

Most numerical schemes applied to solve the advection–diffusion equation are affected by numerical diffusion. Moreover, unphysical results, such as oscillations and negative concentrations, may emerge when an anisotropic dispersion tensor is used, which induces even more severe errors in the solution of multi-species reactive transport. To cope with this long standing problem we propose a modified version of the standard Smoothed Particle Hydrodynamics (SPH) method based on a Moving-Least-Squares-Weighted-Essentially-Non-Oscillatory (MLS-WENO) reconstruction of concentrations. This scheme formulation (called MWSPH) approximates the diffusive fluxes with a Rusanov-type Riemann solver based on high order WENO scheme. We compare the standard SPH with the MWSPH for different a few test cases, considering both homogeneous and heterogeneous flow fields and different anisotropic ratios of the dispersion tensor. We show that, MWSPH is stable and accurate and that it reduces the occurrence of negative concentrations compared to standard SPH. When negative concentrations are observed, their absolute values are several orders of magnitude smaller compared to standard SPH. In addition, MWSPH limits spurious oscillations in the numerical solution more effectively than classical SPH. Convergence analysis shows that MWSPH is computationally more demanding than SPH, but with the payoff a more accurate solution, which in addition is less sensitive to particles position. The latter property simplifies the time consuming and often user dependent procedure to define the initial dislocation of the particles.

© 2015 Elsevier Ltd. All rights reserved.

## 1. Introduction

The numerical solution of the advection–diffusion equation (ADE) is challenging, particularly when the dispersion tensor is anisotropic and when dealing with multispecies reactive solute transport (e.g. [32,58]) and also when the accurate reproduction of the concentration gradients is essential, such as in modeling transport of chemotactic bacteria [39]. More in general, accuracy problems arise when the transformation of transported scalars is controlled by diffusive fluxes, which depend on the complex interplay between diffusion and local concentration gradients [13,15,38,34]. In addition, natural heterogeneity of porous formations results in disordered velocity fields, which vary spatially both in direction and magnitude. Such heterogeneity in the velocity profile leads to plume deformations that greatly enhance spatial variability of solute concentration gradients, thereby fostering local dilution and mixing at both local and global scales. A continuous interplay between sharpening of the concentration gradients due to plume deformation and their smoothing due to diffusion is the main factor shaping the plume and controlling the distribution of solute concentration. Capturing these processes calls for new numerical schemes eliminating or minimizing numerical diffusion and the occurrence of spurious oscillations and negative concentrations.

In an attempt to reduce numerical diffusion arising when classical Eulerian schemes are applied to the ADE, Eulerian–Lagrangian approaches have been developed, in which mass conservation is applied along streamtubes instead than over a structured Eulerian grid (see e.g., [2,5,3,4,14]). Discontinuous Galerkin has also been considered as a possible alternative to Eulerian–Lagrangian schemes. For example, Kim and Wheeler [35,36] proposed a discontinuous Galerkin discretization using mortar finite elements and a multiscale discontinuous Galerkin scheme for the advection–diffusion reaction equation.

Another appealing alternative, which does not suffer from numerical diffusion, is Smoothed Particle Hydrodynamics (SPH), a fully Lagrangian meshless scheme developed by Lucy [40] and Gingold and Monaghan [27] for astrophysics applications, and successively extended to fluid mechanics, such as free surface flows of an incompressible fluid (e.g., [25,41,42]). Successively, Herrera et al. [32] extended SPH to model transport in heterogeneous porous media. Other relevant applications of SPH are those proposed by Tartakovsky and Meakin [50], to model multiphase flow, and by Tartakovsky et al. [51,52] to model solute transport and mineral precipitation in porous and fractured media. Furthermore, Pan et al. [45] combined SPH with continuous boundary force method to solve the Navier–Stokes equations with a Robin boundary condition. The potential of SPH to reduce the impact of numerical dispersion on the numerical solution of ADE in highly heterogeneous formations has been shown by Boso et al. [9].

SPH solves the advective component of the ADE by particle tracking, thereby eliminating numerical diffusion, which in Eulerian schemes arises in the discretization of the advective component, and the diffusive term is solved by using a kernel interpolation approximation. Being a meshless method, SPH does not suffer from grid orientation effects, which is one of the main drawbacks of standard Eulerian schemes [32]. Unlike random walk methods, SPH does not require a background grid to compute concentrations and the numerical precision of the computed concentration is only limited by hardware representation [32,52]. Since particle tracking defines the concentration as the ratio between the mass contained in a cell and its volume, it cannot resolve concentrations smaller those associated to a single particle, which is given by the ratio between the mass of the particle and the volume of the cell. However, SPH may lead to negative concentrations and unphysical oscillations, in particular when the dispersion tensor is anisotropic [29,30,32,44,46,54,55].

In an attempt to reduce the occurrence of unphysical oscillations and negative concentrations, Herrera et al. [32] developed a new hybrid numerical scheme, which applies SPH in a streamline oriented framework. In this scheme, the ADE is written in a local reference system with the longitudinal axis tangent to the streamline, while the dispersion tensor is split into the sum of two tensors. The first tensor originated from the splitting is anisotropic with the transverse component equal to zero, while the second tensor is isotropic. Therefore, the diffusive term originating from the anisotropic tensor is solved by using a one-dimensional finite difference scheme. The second dispersion tensor is diagonal and isotropic and therefore the corresponding diffusive term is solved by standard SPH. Boso et al. [9] proposed a modification of this scheme to take into account the fact that the volume associated to the particles changes along the streamline. With this modification, the method is less prone to develop negative concentrations and is much less demanding in term of computational time than the standard SPH, chiefly because it works with particles which are fixed in space. However, an intrinsic limitation of this method is that it can be applied only to stationary flow fields.

Recently Avesani et al. [6] presented a class of SPH schemes based on a new weighted essentially non-oscillatory (WENO) reconstruction technique on moving points, hereafter referred to as MWSPH, which shows advantages with respect to a traditional SPH scheme in term of accuracy and reduction of unphysical oscillations.

In the present, work we propose and develop a robust numerical scheme to extend MWSPH to the solution of the advection–dispersion equations. Furthermore, we compare the performances of MWSPH and the standard SPH under a few challenging conditions analyzing the occurrence of numerical oscillations and negative concentrations. Finally, we study monotonicity properties of both schemes for different flow fields and degrees of anisotropy of the dispersion tensor, evaluating the occurrence of numerical oscillation and their impact on modeling mixing-controlled reactive solute transport in porous media.

The paper is organized as follows. In Section 2 we introduce the mathematical model for the advection–diffusion equation and describe the standard SPH scheme. In Section 3 we apply MWSPH to the solution of the ADE, describing also WENO reconstruction. In Section 4 we test both the SPH and MWSPH against reference solutions. In Section 5 we apply both schemes to conservative and mixing-controlled reactive transport in heterogeneous porous media, and finally, in Section 6 we drawn some conclusions.

## 2. Smooth Particle Hydrodynamics

We focus on the numerical solution of the ADE for both homogeneous and heterogeneous velocity fields, which is commonly used to model solute transport in porous media:

$$\frac{\partial C}{\partial t} + \mathbf{v} \cdot \nabla C = \nabla \cdot [\mathbf{D} \cdot \nabla C]. \tag{1}$$

The Lagrangian formulation of Eq. (1) assumes the form of a system of an ordinary and a partial differential equation:

$$\frac{d\mathbf{r}(t)}{dt} = \mathbf{v}[\mathbf{r}(t), t], \tag{2}$$

$$\frac{dC(t, \mathbf{r})}{dt} = \nabla \cdot [\mathbf{D}(t, \mathbf{r}) \cdot \nabla C(t, \mathbf{r})], \tag{3}$$

which describe solute transport by advection and dispersion, respectively. The diffusive transport component, defined in Eq. (3), represents dispersion processes at Darcy's scale generated by the interaction between pore diffusion and velocity non uniformity within the pores, while at larger scales the heterogeneity of the velocity field is reproduced directly by the advective term defined in Eq. (2). In Eqs. (2) and (3) $\mathbf{r}$ is the position of the fluid particle, $t$ is time, $\mathbf{v}$ is the fluid velocity, expressed in an Eulerian framework, $\mathbf{D}(t, \mathbf{r})$ is the hydrodynamic dispersion tensor and $C$ is the solute concentration. To simplify the notation, hereafter we consider implicit the dependence of $\mathbf{r}$, $\mathbf{v}$, $C$ and $\mathbf{D}$ from time $t$ and position $\mathbf{r}$. In porous media, the hydrodynamic dispersion tensor assumes the following form (see e.g., [7]:

$$\mathbf{D} = (\alpha_T |v| + D_m) \mathbf{I} + (\alpha_L - \alpha_T) \frac{\mathbf{v} \cdot \mathbf{v}'}{|\mathbf{v}|}, \tag{4}$$

where $D_m$ is the molecular diffusion coefficient, $\alpha_L$ and $\alpha_T$ are the local pore-scale dispersivity coefficients in the directions tangent (longitudinal) and orthogonal (transverse) to the local flow velocity $\mathbf{v}$, respectively. Given Eq. (4) the dispersion tensor becomes diagonal in an orthogonal reference system with the longitudinal axis in the direction of the local velocity, i.e. tangent to the streamline in a steady-state velocity field.

In all SPH based schemes, the system of differential equations (2) and (3) is approximated by using a finite number of points (particles), which carry the physical property of interest, in our case solute concentration, and move with the fluid according to Eq. (2) (see for examples [25,31,42]). We consider here the case in which flow and transport equations are decoupled, such that the flow velocity field is already known when the transport equation is solved. Consequently, Eq. (2), which provides the position of the $i$th particle, can be solved by a standard particle tracking scheme (e.g., [48,49]). Unlike Random Walk Particle Tracking (RWPT) schemes, where the dispersion is modeled with a random movement of particles, SPH uses a kernel interpolation to represent the dispersive term in Eq. (3). Fig. 1 shows a sketch illustrating
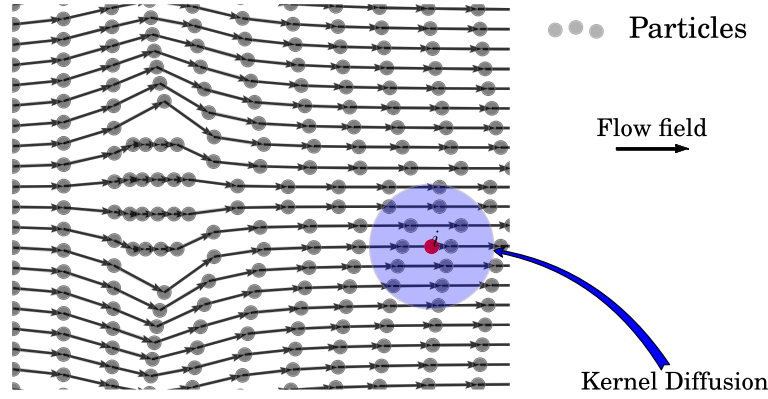
**Fig. 1.** Sketch of the Smooth Particle Hydrodynamic (SPH) scheme in heterogeneous porous media, particle *i* is marked in red. Particles move along streamline and then dispersion is evaluated using a kernel interpolation approximation. (For interpretation of the references to color in this figure legend, the reader is referred to the web version of this article.)

how SPH is applied to the solution of the diffusion term, described by Eq. (3).

### 2.1. SPH discretization of the diffusive term

Español and Revenga [24] derived the following formulation of the diffusive step in SPH, as an extension of the original expression proposed by Brookshaw [10] and further developed by Cleary and Monaghan [16] (see [42] for a complete review) to model thermal dispersion:

$$\frac{dC_i}{dt} = \frac{1}{2}\sum_{j}^{N}\frac{m_j}{\rho_{ij}}(C_i - C_j)\nabla_i W_{ij}\mathcal{D}(r_i, r_j), \tag{5}$$

where

$$\mathcal{D}(r_i, r_j) = \sum_{l=1}^{v}\sum_{k=1}^{v}\left(D_{lk}^i + D_{lk}^j\right)\left[4\frac{(r_j - r_i)_l(r_j - r_i)_k}{|r_j - r_i|^2}\right] - \delta_{lk}. \tag{6}$$

The terms $C_i$ and $C_j$ are the solute concentration of the *i*th and *j*th particles, at positions $\mathbf{r}_i$ and $\mathbf{r}_j$, respectively. In Eqs. (5) and (6) $m_i$ is the mass of *i*th particle, $\nabla_i W_{ij}$ is the gradient of the interpolating kernel function centered in $\mathbf{r}_i$ [25] and $v$ indicates space dimensionality. In addition, $D_{lk}$ indicate the component $l$, $k$ of the dispersion tensor and $\delta_{lk}$ is the Kronecker's delta. Here, $\rho_{ij} = (\rho_i + \rho_j)/2$, where $\rho_i$ is the density of the $i$–th particle, with the arithmetic average introduced to ensure that the diffusive fluxes are antisymmetric [31]. For the interpolating kernel function we choose, among the different possibilities, the following cubic *B*-spline:

$$W_{ij} = \frac{c}{(h_{ij})^v}\begin{cases} 2/3 - q_{ij}^2 + q_{ij}^3/2 & \text{if } 0 \leqslant q_{ij} < 1, \\ (2 - q_{ij})^3/6 & \text{if } 1 \leqslant q_{ij} < 2, \\ 0 & \text{if } q_{ij} \geqslant 2, \end{cases} \tag{7}$$

where $q_{ij} = |\mathbf{r}_i - \mathbf{r}_j|/h_{ij}$ is the relative distance between particles *i* and *j*, while *c* is a normalization constant selected in such a way that the volume integral of the kernel function in $\mathbf{R}^v$ is equal to one (a detailed explanation is available in [25,42]). In addition, $h_{ij}$ is the smoothing length and determines the size of the kernel support for each particle, which is locally variable and defined as:

$$h_{ij} = \frac{1}{2}(h_i + h_j), \quad \text{with} \quad h_i = \sigma\sqrt[v]{\frac{m_j}{\rho_j}}, \tag{8}$$

where $\sigma$ is a constant selected to have at least 40–50 interpolation particles within the compact support with $\sigma = 2$ [6].

### 3. The MWSPH formulation of advection–dispersion equations

Following the new class of MWSPH schemes developed by Avesani et al. [6], we propose to use Riemann solvers to estimate diffusive fluxes:

$$\frac{dV_i}{dt} = \sum_{j=1}^{N}2V_iV_j(\overline{\mathbf{v}}_{ij} - \mathbf{v}_i) \cdot \nabla W_{ij}, \tag{9}$$

$$\frac{dV_iC_i}{dt} = \sum_{j=1}^{N}2V_iV_j\underline{\mathbf{G}}_{ij} \cdot \nabla W_{ij}, \tag{10}$$

where $\underline{\mathbf{G}}_{ij}$ is the flux tensor, $V_i$ is the volume of the particle *i*, which evolves in time according to Eq. (9), and $\overline{\mathbf{v}}_{ij}$ is the velocity at the interface between the two interacting particles $\mathcal{P}_i$ and $\mathcal{P}_j$. The flux tensor $\underline{\mathbf{G}}_{ij}$ is approximated by using a Rieman solver. Considering the Rusanov solver, the flux tensor assumes the following expression [21,33]:

$$\underline{\mathbf{G}}_{ij} = \frac{1}{2}\left(\mathbf{F}(\nabla C_{ij}^+) + \mathbf{F}(\nabla C_{ij}^-)\right) - \Theta(C_{ij}^- - C_{ij}^+) \otimes \mathbf{n}_{ij}, \tag{11}$$

where $\mathbf{F}$ is the non-linear flux vector, which depends on the concentration and the concentration gradient, $\Theta$ is the maximum of the Jacobian matrix of the flux with respect to the gradient of $C$ [26,33], i.e the maximum eigenvalue of $\partial\mathbf{F}(\nabla C)/\partial\nabla C$, and $\mathbf{n}_{ij}$ is the unitary separation vector between particles *i* and *j*. Furthermore, $C_{ij}^- = C_i(\overline{\mathbf{r}}_{ij})$, $C_{ij}^+ = C_j(\overline{\mathbf{r}}_{ij})$, $\nabla C_i^- = \nabla C_i(\overline{\mathbf{r}}_{ij})$ and $\nabla C_j^+ = \nabla C_j(\overline{\mathbf{r}}_{ij})$ are the concentrations and concentration gradients computed at the midpoint, $\overline{\mathbf{r}}_{ij} = (\mathbf{r}_i + \mathbf{r}_j)/2$, of the segment connecting the particles *i* and *j* using local high-order reconstruction at $\mathbf{r}_i$ and $\mathbf{r}_j$, given the concentrations of the surrounding particles. As shown in Fig. 2(b) and (a), local high-order reconstruction polynomials $C_i(\mathbf{r})$ and $C_j(\mathbf{r})$ are first defined for each pair of interacting particles $\mathcal{P}_i$ and $\mathcal{P}_j$ and used successively to compute the concentrations and the concentration gradients at the midpoint of the segment connecting the two particles. After these preparatory steps, the flux $\underline{\mathbf{G}}_{ij}$ (10) between two interacting particles assumes the following expression:

$$\underline{\mathbf{G}}_{ij} = \frac{1}{2}(\underline{\mathbf{D}}_{ij}^-\nabla C_{ij}^- + \underline{\mathbf{D}}_{ij}^+\nabla C_{ij}^+) - \Theta_{ij}(C_{ij}^+ - C_{ij}^-) \otimes \mathbf{n}_{ij}, \tag{12}$$

where $\underline{\mathbf{D}}_{ij}$ is the dispersion tensor evaluated at the interface between interacting particles *i* and *j*. The local high-order reconstruction polynomials $C_i(\mathbf{r}_{ij})$ are computed for each particle $\mathcal{P}_i$ with a nonlinear meshfree Moving-Least-Squares WENO reconstruction,
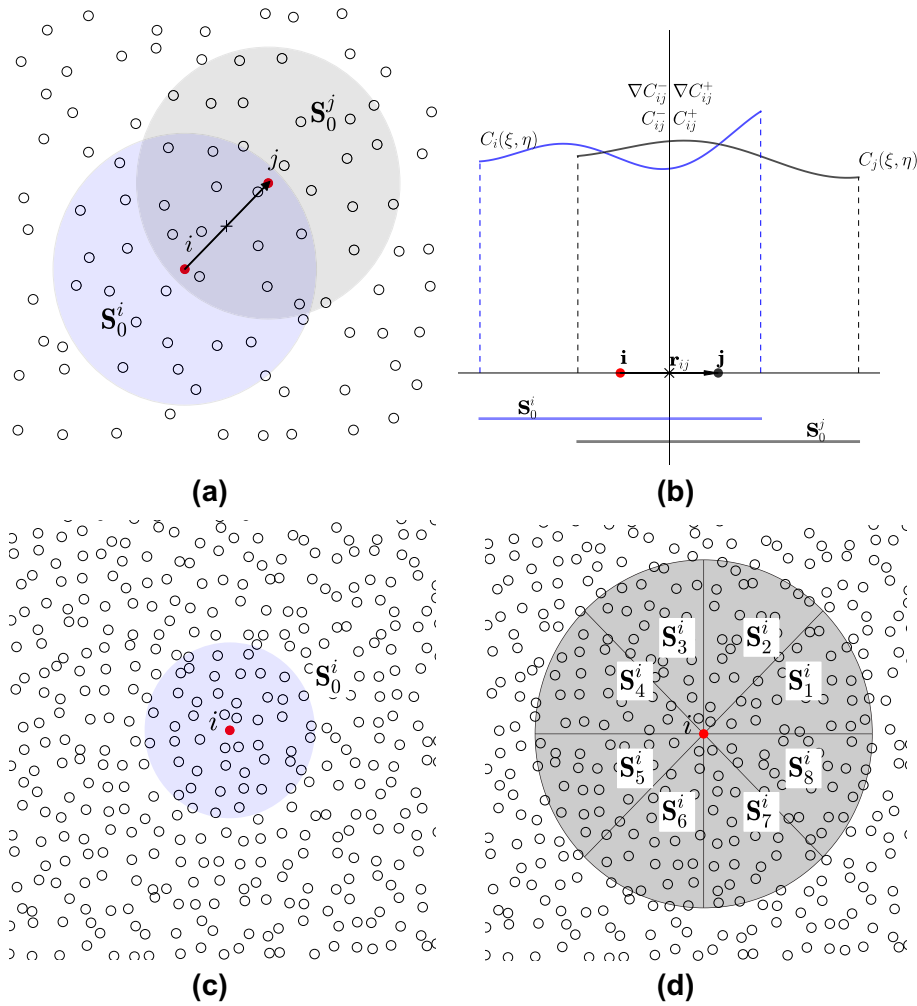
**Fig. 2.** Sketch of the particle stencils and reconstruction polynomials.

knowing the concentration of particles $\mathcal{P}_j$ in its surrounding. Details on the application of this scheme are provided in the work by Avesani et al. [6]. Here we summarize the main steps of the procedure.

First, a set of reconstruction stencils is constructed for each particle $\mathcal{P}_i$ as follows:

$$\mathcal{S}_s^i = \bigcup_k^{ne_s} \mathcal{P}_{j(k)}, \tag{13}$$

where $k$ (with $1 \leqslant k \leqslant ne_s$) is a local index, counting the particles $\mathcal{P}_j$ in each stencil, $j = j(k)$ is the mapping from the local index $k$ to the global indexation of the particles in the computational domain $\Omega$ and $ne_s$ is the number of particles in each stencil. The set of stencils consists of one central stencil $\mathcal{S}_0^i$ (Fig. 2(c)) and a set of 8 one-sided stencils ($1 \leqslant s \leqslant 8$, Fig. 2(d)). The central stencil is obtained by the union of the central particle $\mathcal{P}_i$ and its surrounding particles $\mathcal{P}_j$ as follows:

$$\mathcal{S}_0^i = \bigcup_k^{ne_s} \mathcal{P}_{j(k)}, \quad \|\mathbf{r}_{ij}\| \leqslant h_{mls}, \tag{14}$$

while the one-sided stencils are defined as:

$$\mathcal{S}_s^i = \bigcup_k^{ne_s} \mathcal{P}_{j(k)}, \quad \|\mathbf{r}_{ij}\| \leqslant 2h_{mls} \quad \text{and} \quad \theta \in [(s-1)\pi/4, s\pi/4], \tag{15}$$

where $h_{i,mls}$ is a characteristic length and $\theta$ is the angle that the vector $\mathbf{r}_{ij} = \mathbf{r}_j - \mathbf{r}_i$ connecting the two particles $\mathcal{P}_i$ and $\mathcal{P}_j$ forms with the $x$-axis:

$$\tan(\theta) = \frac{y_j - y_i}{x_j - x_i}. \tag{16}$$

The smoothing length $h_{i,mls}$ is locally variable and assumes the following expression:

$$h_{i,mls} = \sigma_{mls} \sqrt{m_i/\rho_i} \tag{17}$$

with a $\sigma_{mls}$ being a suitable constant.

The second step of the procedure concerns with the reconstruction of the local concentration, through the following nine polynomials:

$$C_i^s(\xi, \eta) = C_i + \sum_{m=1}^{nc-1} \widehat{w}_{m,s} \phi_m(\xi, \eta), \tag{18}$$

one for each of the nine stencils $\mathcal{S}_s^{p_i}$, $s = 0, \ldots, 8$, previously defined and represented in Fig. 2(d). The form of the polynomials depends on space dimensionality, where $C_i^s(\xi, \eta)$ for the $i$th in the $s$th stencil. For simplicity hereafter we consider two-dimensional applications, but the reconstruction procedure can be easily extended to three-dimensional applications. Therefore, considering two-dimensional polynomials, $\xi = (x - x_i)/h_{mls}$ and $\eta = (y - y_i)/h_{mls}$ are the local

coordinates centered at the $i$th particle, $\widehat{w}_{m,s}$ denotes the set of $nc = (M+2)(M+1)/2$ undetermined coefficients of the $s$-$th$ polynomial and $\phi_m$ are the associated basis functions. Eq. (18) is the Taylor series expansion of order $M$ of the concentration around $(x_i, y_i)$, i.e. the position of the $i$th particle. Finally, the $nc$ basis functions in Eq. (18) are defined as follows:

$$\phi_m(\xi, \eta) = \frac{\xi^a \eta^b}{h_{mls}^{(a+b)}}, \tag{19}$$

where $a + b = l$, and $l$ ranges from 1 to $M$ [1,59]. The unknown coefficients $\widehat{w}_{m,s}$ are computed applying the set of reconstruction equations on each stencil $S_s$:

$$C_j - C_i = \sum_{m=1}^{nc-1} \widehat{w}_{m,s} \phi_m(\xi_j, \eta_j), \quad \forall \mathcal{P}_j \in S_s^i. \tag{20}$$

The number of particles $ne_s$ in each stencil $S_s$, and therefore the number of Equations in the system (20), is chosen such that $ne_s > nc$. Consequently, Eq. (20) constitute an overdetermined linear algebraic system for the $nc$ coefficients of the polynomials, which is solved by least square minimization of the residual between particles concentration and the corresponding values provided by the interpolating polynomials at the particles locations [1,22]. The minimum number of particles in each stencil is set to $2nc$ to ensure linear stability [22,23].

The final non-linear WENO reconstruction polynomial $C_{i,WENO}(\xi, \eta)$ of degree $M$ is obtained by a non-linear combination of the nine polynomials $C_i^s$ of order $M$ reconstructed on the $ns$ stencils:

**Table 1**
Parameters used in the homogeneous test case.

| Parameter | Symbol | Value |
|---|---|---|
| Length numerical domain | $L$ | 50 |
| Peclét number | $Pe$ | 10 |
| ratio between transverse and longitudinal dispersivity | $\lambda = \alpha_T/\alpha_L$ | 0.1 |

$$C_{i,WENO}(\xi, \eta) = \sum_{l=1}^{ns} C_i^s(\xi, \eta) \tag{21}$$

with the normalized nonlinear weights

$$\omega_l = \frac{\widetilde{\omega_l}}{\sum_{r=1}^{ns} \widetilde{\omega}_r} \tag{22}$$

computed from the non-normalized weights $\widetilde{\omega}_l$ as [22,23]:

$$\widetilde{\omega}_l = \frac{\lambda_r}{(\epsilon + \sigma_s)^r}, \tag{23}$$

where $\epsilon = 10^{-14}$, $r = 4$ and the linear weights are set $\lambda_0 = 10^5$ for the central stencil and $\lambda_l = 1$ for the one side stencil ($1 \leqslant l \leqslant 8$). The smoothness indicator is computed in a mesh-independent manner as [6]:

$$\sigma_s = \sum_{1 \leqslant |m| \leqslant M} \hat{\mathbf{w}}_{m,s}^2, \tag{24}$$

where the integration of the derivatives in the central cell is implicitly taken into account. Once defined the WENO reconstruction



**(a)** *2D concentration distribution.*



**(b)** *Section forming the angle 0 with the x−axes*



**(c)** *Section forming the angle $\pi/4$ with the x−axes*



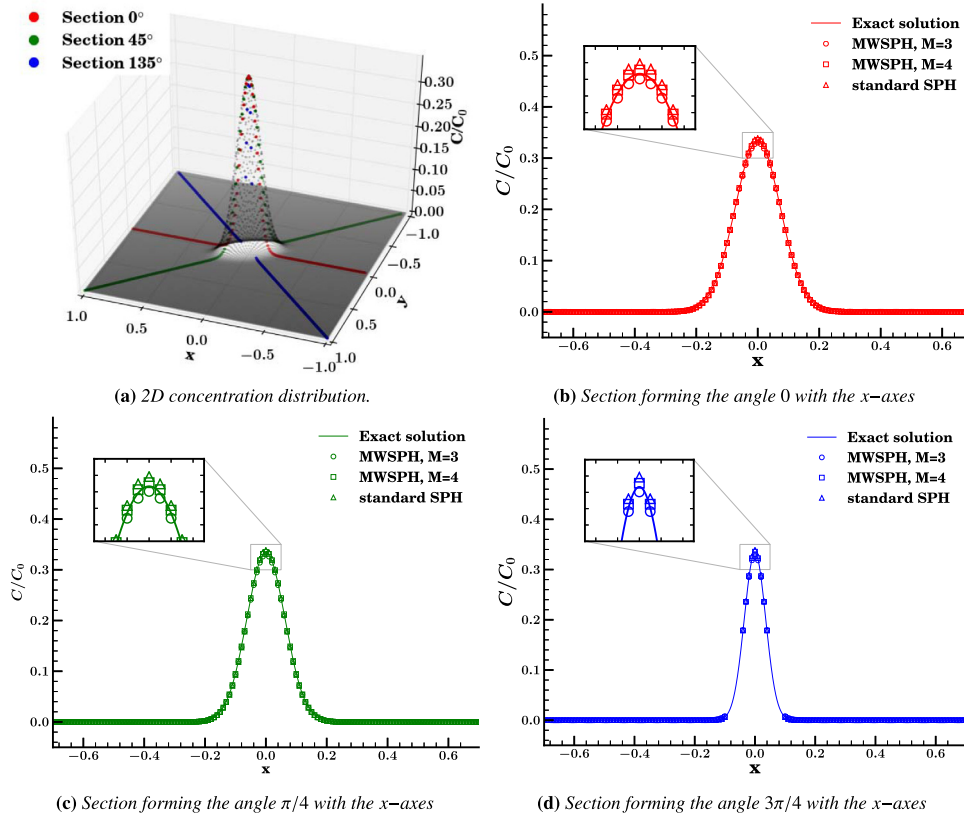**(d)** *Section forming the angle $3\pi/4$ with the x−axes*

**Fig. 3.** Comparison of exact and numerical solutions for uniformly distributed particles at dimensionless time $t = 5$ obtained with standard SPH and MWSPH with third (MWSPH-M3)- and fourth (MWSPH-M4)-order reconstruction. The concentration is also shown along three sections forming an angle of 0, $\pi/4$ and $3\pi/4$ with respect to the longitudinal axes $x$ in a uniform velocity field with direction inclined of $\beta = \pi/6$ with respect to the same axes. Numerical solutions are shown for $\sigma = 2.5$, $\sigma_{mls} = 4.5$, $CFL = 0.9$, $201 \times 201$ particles.

polynomial for the concentration, the gradient reconstruction polynomial is directly computed from the derivatives of the basis functions as follows:

$$\nabla C_{i,WENO}(\xi, \eta) = \sum_{m=1}^{nc} \hat{w}_m J^{-T} \nabla_\xi \phi_m \tag{25}$$

with

$$\nabla_\xi = \left(\frac{\partial}{\partial \xi}, \frac{\partial}{\partial \eta}\right)^T. \tag{26}$$

The reader can notice that, MWSPH is written in conservative form [6], this means that, as in the standard SPH, the global mass of solutes is conserved exactly if a kernel gradient correction is not applied. Otherwise, the gradients of the kernel are no longer anti-symmetric and both standard SPH and MWSPH do not guarantee conservation of mass [56].
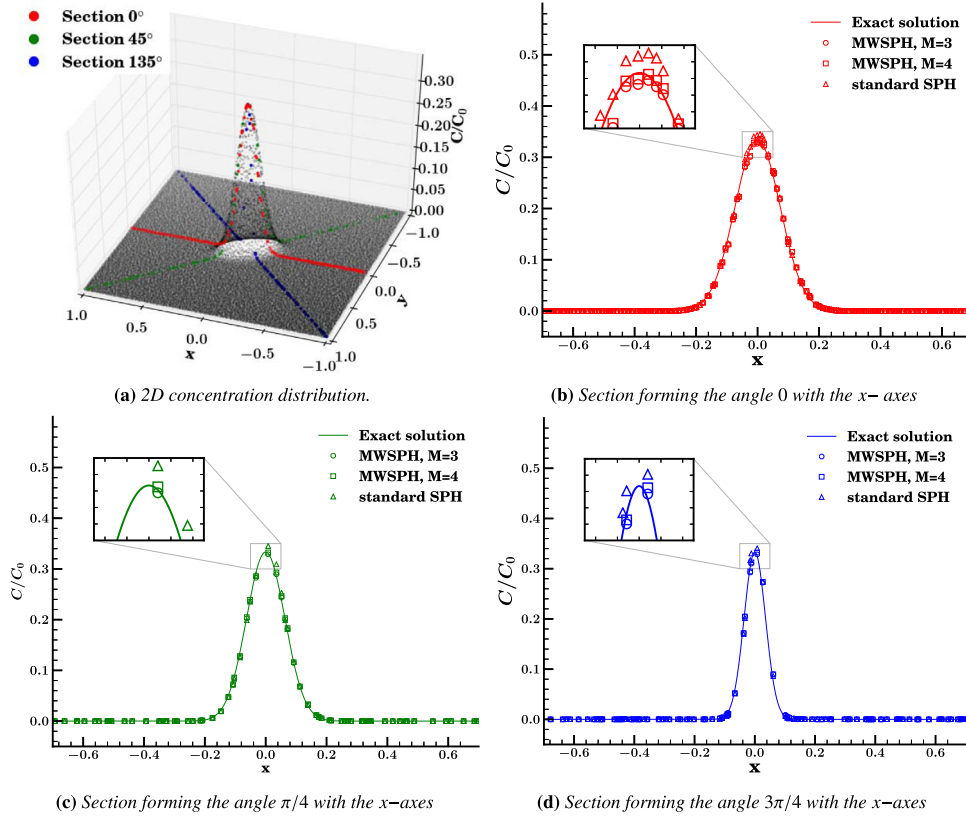


**(a)** *2D concentration distribution.*

**(b)** *Section forming the angle 0 with the x− axes*

**(c)** *Section forming the angle π/4 with the x−axes*

**(d)** *Section forming the angle 3π/4 with the x−axes*

**Fig. 4.** Comparison with the analytical solution of the numerical solutions for irregularly distributed particles at time $t = 5$ obtained with standard SPH and both MWSPH-M3 and MWSPH-M4. The concentration is also shown along three sections inclined of 0, $\pi/4$ and $3\pi/4$ with respect to axes $x$ in a uniform velocity field with direction forming an angle $\beta = \pi/6$ with respect to the longitudinal direction. Numerical solutions are shown for $\sigma = 2.5$, $\sigma_{mls} = 4.5$ and $CFL = 0.9$, $201 \times 201$ particles.
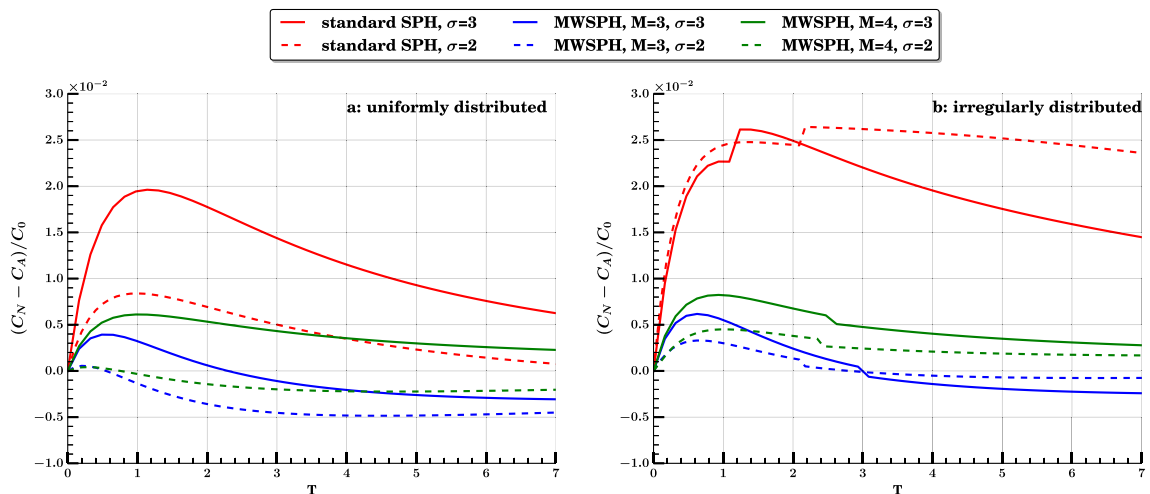


**Fig. 5.** Difference between the maximum concentration of numerical ($C_N$) and analytical ($C_A$) solutions as function of time for (a) uniformly distributed and (b) irregularly distributed particles. Numerical solutions obtained with SPH, MWSPH-M3 and MWSPH-M4 are for $\sigma = 2$ and 3, $\sigma_{mls} = 4.5$ and $CFL = 0.9$.

## 4. Comparison between SPH and MWSPH

### 4.1. Accuracy of the numerical schemes

The aim of this section is to compare accuracy and positivity preserving properties of MWSPH and standard SPH for transport of a conservative solute in a homogeneous flow field. Hereafter, MWSPH-M3 and MWSPH-M4 indicate the MWSPH scheme with third and fourth-order flux reconstruction, respectively. In the present work we adopt the third order TVD Runge–Kutta scheme [28] under the Courant–Friedrichs–Lewy (CFL) condition [17].

We consider transport of a non reactive solute instantaneously injected at time $t = 0$ according to the following spatial distribution:

$$C(x, y, t = 0) = \frac{M}{2\pi w^2 b} \exp\left[-\frac{x^2 + y^2}{2w^2}\right], \qquad (27)$$

where, $M$ is the mass injected, $b$ is the thickness and $w$ is the characteristic size of the slug injection. The velocity field $\mathbf{v}$ is assumed uniform and forming an angle $\beta$ with the axis $x$. In an unbounded domain the solution of the ADE (1) with the initial condition (27) assumes the following expression:

$$C(x, y, t)/C_0 = \frac{1}{2\pi\sigma} \exp$$
$$\times \left[-\frac{(x-x_0)^2(1+2D_{yy}t) + (y-y_0)^2(1+2D_{xx}t) - 4D_{xy}t(x-x_0)(y-y_0)}{2\sigma^2}\right],$$
(28)

where $\sigma = \sqrt{1 + 2t\left[D_{xx} + D_{yy} - 2\left(D_{xy}^2 - D_{xx}D_{yy}\right)t\right]}$. Hereafter, length are dimensionless with respect to $w$, time with respect to the advective characteristic time $T = w/v$, the dispersion coefficients $D_{ij}$, $i, j = x, y$ with respect to the product $vw$ and the concentration with respect to the maximum concentration $C_0 = M/(w^2 b)$.
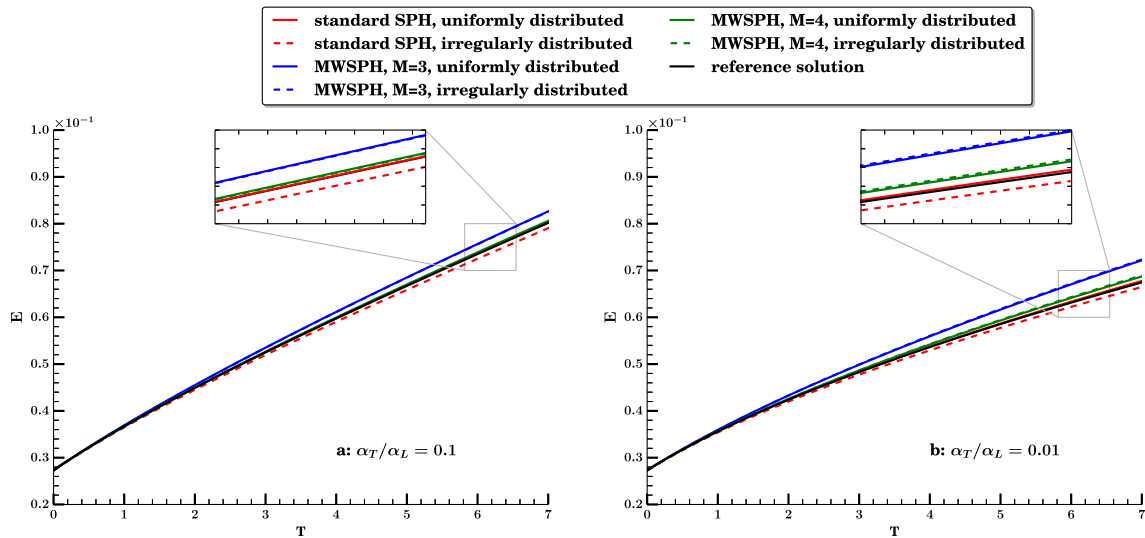


Fig. 6. Dilution index $E$ computed with the concentration distribution provided by SPH, MWSPH-M3 and MWSPH-M4 for uniformly and irregularly distributed particles and for $\lambda = \alpha_T/\alpha_L$ equal to (a) 0.1 and (b) 0.01. In all cases, $\sigma_{mls} = 4.5$, $CFL = 0.9$ and $\sigma = 3$.
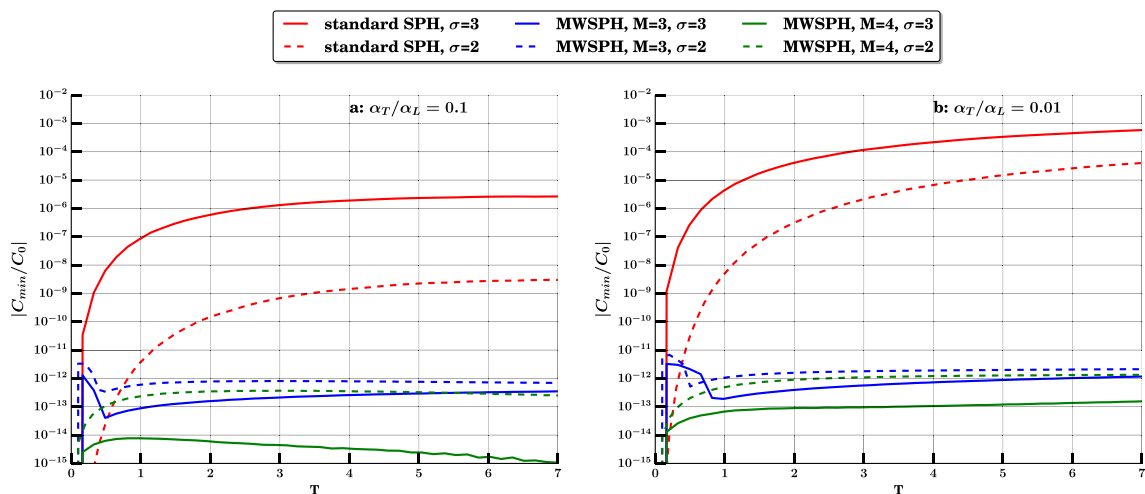


Fig. 7. Maximum absolute value of the negative concentrations obtained with SPH, MWSPH-M3 and MWSPH-M4 with (a) $\lambda = \alpha_T/\alpha_L$ equal to (a) 0.1 and (b) 0.01, for $\sigma = 2$ and 3, $\sigma_{mls} = 4.5$ and $CFL = 0.9$. The concentration is normalized with respect to the initial concentration $C_0$ and it is shown in logarithmic scale.

In Eq. (28) $x_0 = t\cos\beta$, $y_0 = t\sin\beta$ and the three components of the dispersion tensor assume the following expressions (see e.g., [7]):

$$D_{xx} = \frac{1 + (1-\lambda)\cos^2\beta}{Pe}, \quad D_{yy} = \frac{1 + (1-\lambda)\sin^2\beta}{Pe},$$
$$D_{xy} = \frac{(1-\lambda)\sin\beta\cos\beta}{Pe}, \tag{29}$$

where $Pe = w/\alpha_L$ is the Peclét number, defined with respect to the longitudinal dispersivity and $\lambda = \alpha_T/\alpha_L$ is the ratio between transverse and horizontal dispersivities.

Since in a homogeneous flow field the relative position of the particles does not change in time, we focus on the solution of the dispersive fluxes by setting $x_0 = y_0 = 0$ into Eq. (28) such that the maximum concentration is located at $(x, y) = (0, 0)$. Furthermore, we apply the two SPH schemes by considering particles both uniformly and irregularly distributed within the computational domain. The irregular distribution is obtained by perturbing the position of the particles at the nodes of the regular grid with spacing $\Delta x$ and $\Delta y$ used in the uniform case by the following quantities: $\epsilon_1 \Delta x$ and $\epsilon_2 \Delta y$, where $\epsilon_1$ and $\epsilon_2$ are two independent random numbers drawn from a uniform distribution within the range $[0, 1]$. Table 1 shows the parameters used for this test case. Notice that
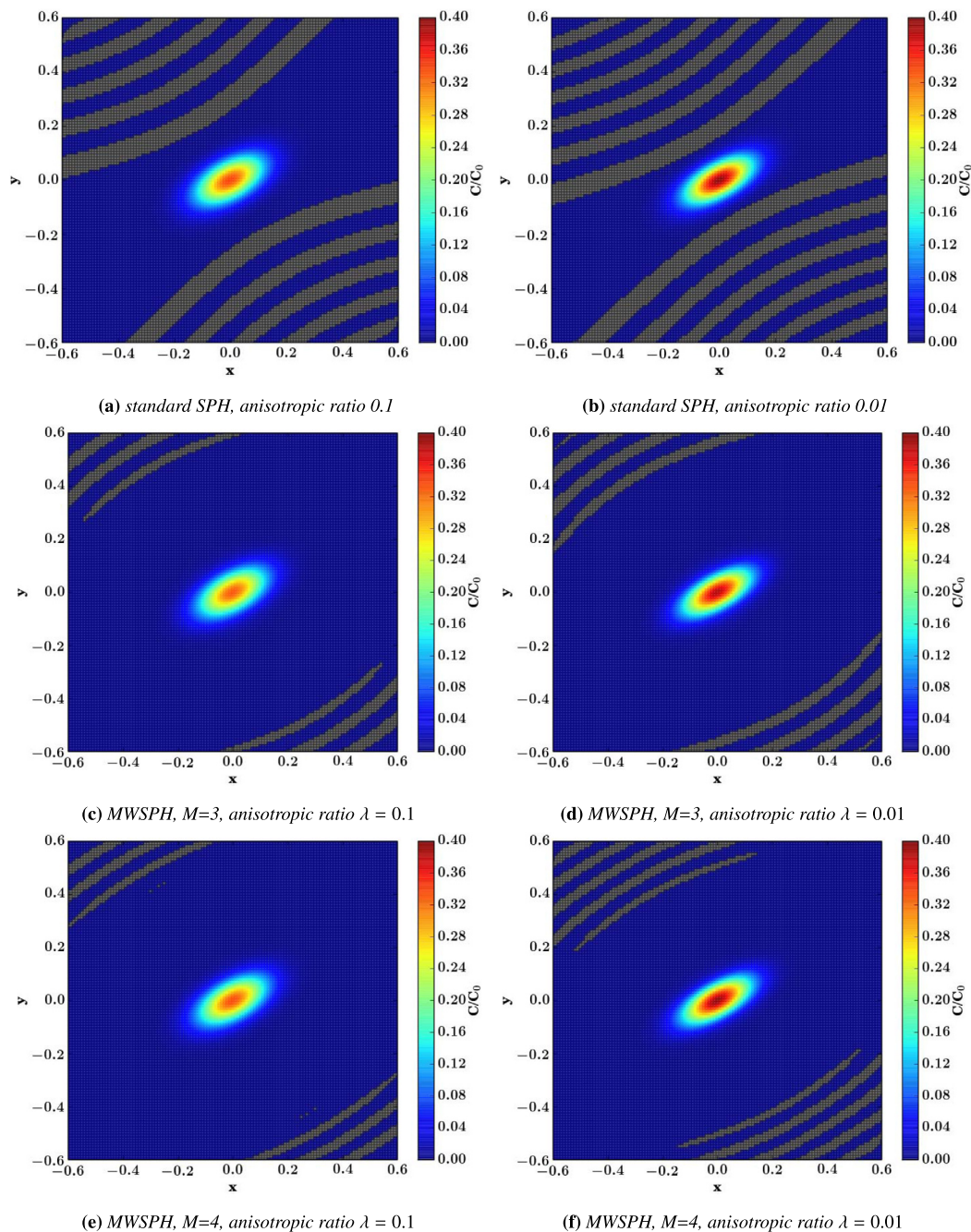


(a) standard SPH, anisotropic ratio 0.1

(b) standard SPH, anisotropic ratio 0.01

(c) MWSPH, M=3, anisotropic ratio $\lambda = 0.1$

(d) MWSPH, M=3, anisotropic ratio $\lambda = 0.01$

(e) MWSPH, M=4, anisotropic ratio $\lambda = 0.1$

(f) MWSPH, M=4, anisotropic ratio $\lambda = 0.01$

**Fig. 8.** Concentration distribution at dimensionless time $t = 10$ computed with SPH (first row), MWSPH-M3 (second row) and MWSPH-M4 (third row), for $\lambda = 0.1$ (left column) and $\lambda = 0.01$ (right column), by using $201 \times 201$ uniformly distributed particles. In all cases $\sigma = 3.0$, $\sigma_{mls} = 4.5$, $CFL = 0.9$ and $\beta = \pi/6$. Negative concentrations are indicated in gray.
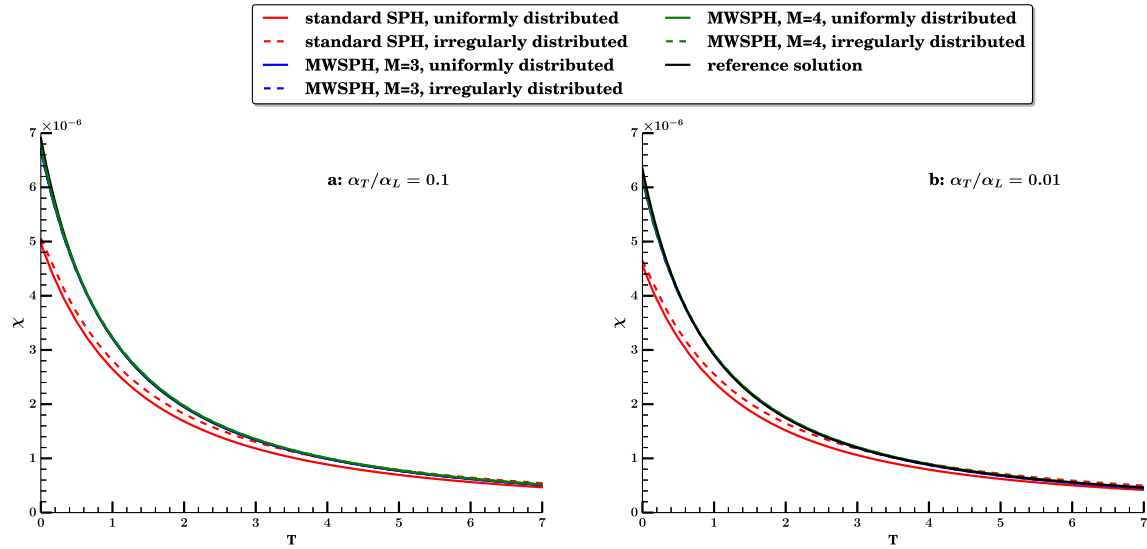
**Fig. 9.** Dissipation rate $\chi$ computed with the concentration distribution provided by SPH, MWSPH-M3 and MWSPH-M4 for uniformly and irregularly distributed particles and for (a) $\lambda = 0.1$ and (b) $\lambda = 0.01$. In all cases $\sigma_{mls} = 4.5$, $CFL = 0.9$ and $\sigma = 3$.

**Table 2**

Convergence test for anisotropic dispersion test case with standard SPH, MWSPH-M3 and MWSPH-M4. The first column report the dimensionless spacing $\Delta x$ between particles, the following three columns the norms $L_1$, $L_2$ and $L_\infty$ used to assess the error, which are followed by the rate of convergence evaluated with respect to the spacing between particles of the previous row. The last column gives the CPU time of the serial code on Intel(R) Core(TM) i7-2640M CPU 2.80 GHz with 8 GB of RAM. The error norms refer to the concentration considering uniformly distributed particles for the homogeneous test case at time $t = 1$.

| $\Delta x$ | $\epsilon_{L_1}$ | $\epsilon_{L_2}$ | $\epsilon_{L_\infty}$ | $\mathcal{O}(L_1)$ | $\mathcal{O}(L_2)$ | $\mathcal{O}(L_\infty)$ | $t_{CPU}(s)$ |
|---|---|---|---|---|---|---|---|
| *Standard SPH ($\sigma = 3.0$)* | | | | | | | |
| 0.20E−01 | 0.10E−03 | 0.11E−04 | 0.29E−01 | – | – | – | 3.84 |
| 0.10E−01 | 0.33E−04 | 0.17E−05 | 0.75E−02 | 1.66 | 2.74 | 1.96 | 26.17 |
| 0.50E−02 | 0.17E−04 | 0.42E−06 | 0.34E−02 | 0.94 | 2.03 | 1.14 | 250.96 |
| 0.25E−02 | 0.15E−04 | 0.17E−06 | 0.25E−02 | 0.18 | 0.13 | 0.44 | 17718.67 |
| *MWSPH M = 3 ($\sigma = 3.0$)* | | | | | | | |
| 0.20E−01 | 0.15E−03 | 0.13E−04 | 0.29E−01 | – | – | – | 197.11 |
| 0.10E−01 | 0.29E−04 | 0.13E−05 | 0.64E−02 | 2.34 | 3.24 | 2.17 | 1731.15 |
| 0.50E−02 | 0.37E−05 | 0.10E−06 | 0.95E−03 | 3.01 | 3.76 | 2.76 | 18491.27 |
| 0.25E−02 | 0.11E−05 | 0.17E−07 | 0.40E−03 | 1.75 | 2.55 | 1.25 | 158064.79 |
| *MWSPH M = 4 ($\sigma = 3.0$)* | | | | | | | |
| 0.20E−01 | 0.15E−03 | 0.13E−04 | 0.29E−01 | – | – | – | 222.82 |
| 0.10E−01 | 0.29E−04 | 0.13E−05 | 0.64E−02 | 2.36 | 3.18 | 2.17 | 1996.12 |
| 0.50E−02 | 0.37E−05 | 0.10E−06 | 0.95E−03 | 3.24 | 3.00 | 1.76 | 19459.43 |
| 0.25E−02 | 0.11E−05 | 0.17E−07 | 0.40E−03 | 1.53 | 2.40 | 1.20 | 212704.79 |
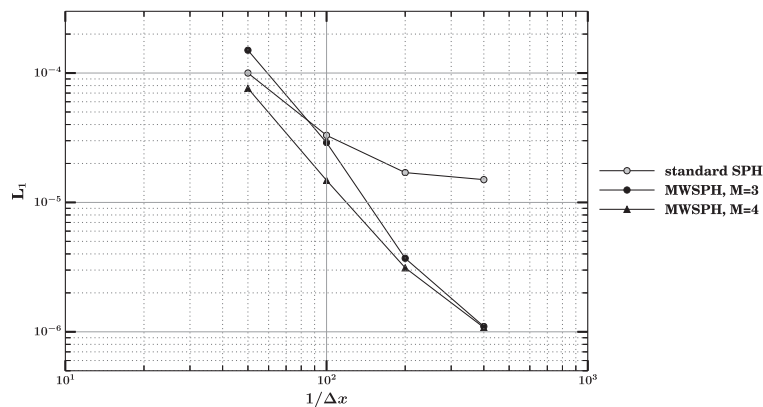


**Fig. 10.** Error norm $L_1$ computed for the homogeneous test case with uniformly distributed particles, for $\sigma = 3$, $CFL = 0.9$, with $\Delta x$ being the distance between the particles.

the selected anisotropy ratio of the dispersivity tensor is $\lambda = 0.1$, which is in line with what observed in experimental studies [7, Section 5.2.2] and similar to the value used by Herrera and Beckie [30].

Fig. 3(a)–(d) compare the concentration distribution obtained by SPH and MWSPH with the exact analytical solution (28). In particular, Fig. 3(a) shows the three-dimensional view of the numerical and analytical solutions, while Fig. 3(b)–(d) shows the same solutions along the three sections shown in Fig. 3(a), which form the angles 0°, 45° and 135° with the x direction. The three numerical schemes agrees quite well, with MWSPH-M4 showing the best match to the analytical solution, with respect to the other two schemes, though the differences are small everywhere. However, the concentration peak is slightly underestimated by MWSPH-M3 and overestimated by SPH.

The case with an irregular spatial distribution of the particles is shown Fig. 4(a)–(d). Here the advantage of using MWSPH instead of SPH is more evident than for uniform particles distribution. The relative error is much smaller for MWSPH-M3 than SPH, though in absolute terms the difference is small also for SPH. The substantial insensitivity of MWSPH to the spatial distribution of particle density is an appreciable property in modeling transport, in particular for heterogeneous velocity fields, which create an irregular distribution of the particles with significant rarefaction behind (with respect to flow direction) areas of low velocity.

Fig. 5 shows the evolution in time of the relative difference between the maximum concentration obtained with the numerical solutions and the corresponding exact analytical solution. The comparison is shown for standard SPH, MWSPH-M3 and MWSPH-M4 with smoothing length set to $\sigma = 3$ and 2. As reported by Herrera [29] and evidenced in Figs. 3 and 4, standard SPH overestimates the maximum concentration. When the particles are uniformly distributed both MWSPH-M3 and MWSPH-M4 perform much better than SPH at early times, with relative errors smaller than 0.6% and 2%, respectively. Standard SPH is very sensitive to the choice of the smoothing length, with the maximum relative error that drops from 2% to 0.8% when $\sigma$ is reduced from 3 to 2. Both MWSPH schemes are much less sensitive to the smoothing length, though the shorter the smoothing length, the smaller the error at all explored times (see how dashed blue and green lines compare with solid lines of the same color). The performance of the two MWSPH schemes deteriorate much less than SPH when the spatial distribution of particles becomes irregular, and in this case SPH does not significantly improve its performance by reducing the smoothing length, as can be observed by comparing Fig. 5(b) with Fig. 5(a). The results obtained with MWSPH are rather insensitive to the choice of the order of the polynomial interpolation for concentration reconstruction, and to the particles spatial distributions, with the latter property resolving the major drawback of SPH when applied to the solution of the ADE in a heterogeneous velocity field.
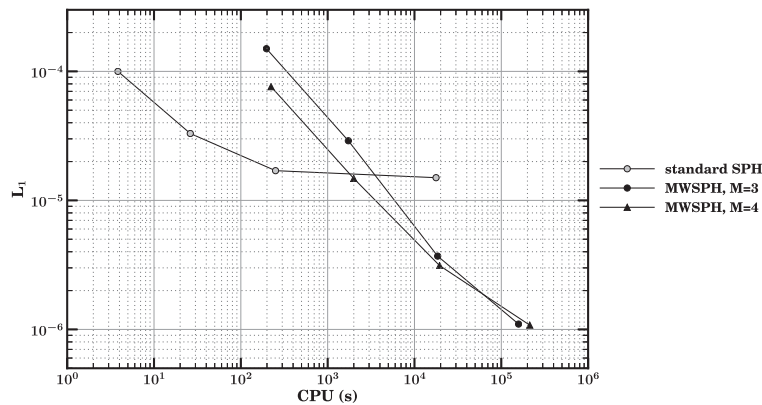


**Fig. 11.** Error norm $L_1$, computed for homogeneous test case with uniformly distributed particles, versus the computational time for a single processor Intel(R) Core(TM) i7-2640M CPU 2.80 GHz.



(a) *Flow field*  (b) *Initial conditions and particle positions*
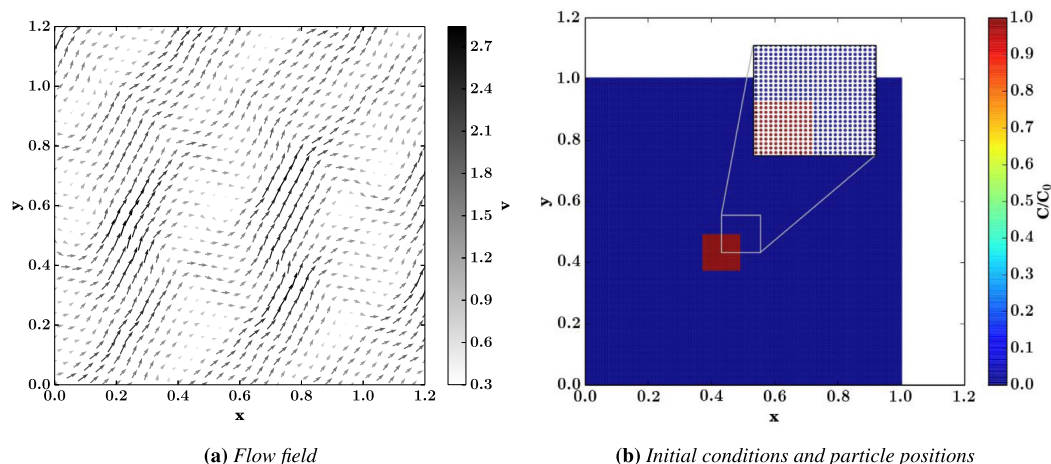
**Fig. 12.** (a) Flow velocity field for the heterogeneous test case and (b) sketch of the computational domain with indicated the source area and the initial distribution of the particles.
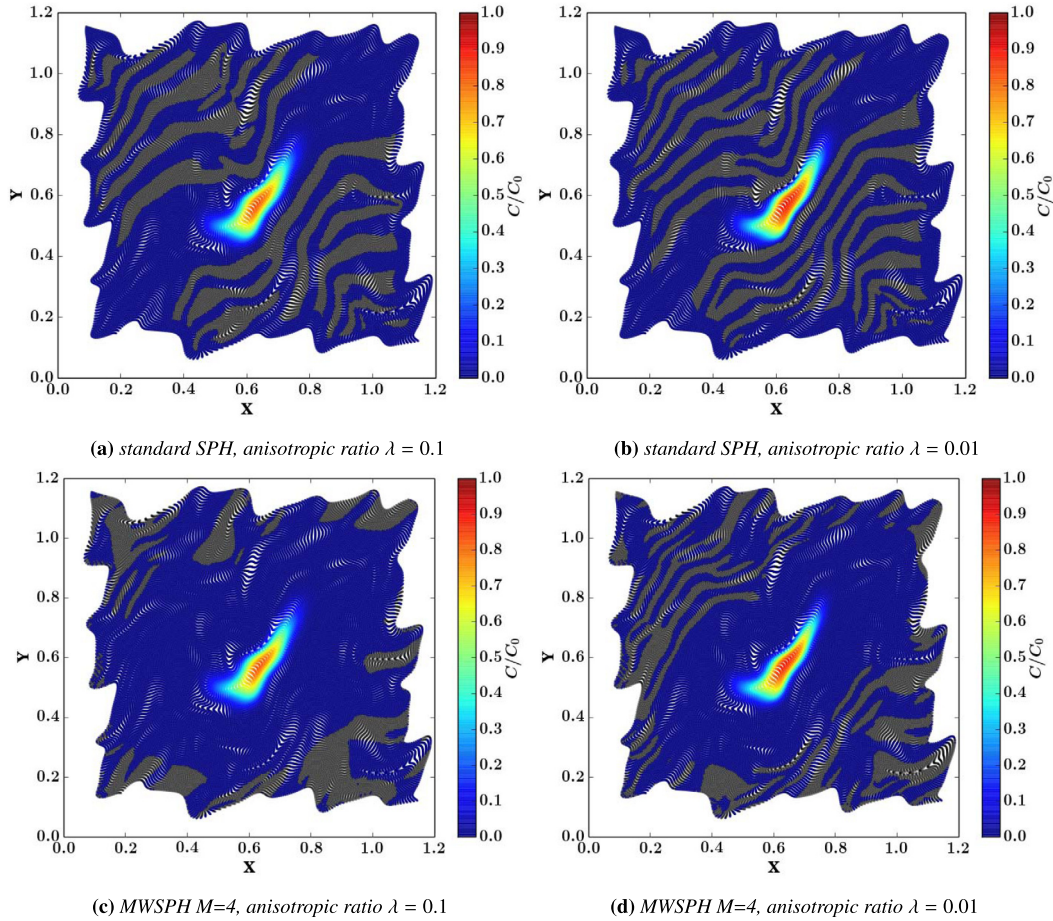
**(a)** *standard SPH, anisotropic ratio $\lambda = 0.1$*

**(b)** *standard SPH, anisotropic ratio $\lambda = 0.01$*

**(c)** *MWSPH M=4, anisotropic ratio $\lambda = 0.1$*

**(d)** *MWSPH M=4, anisotropic ratio $\lambda = 0.01$*

**Fig. 13.** Concentration distribution at dimensionless time $t = 12$, computed for the heterogeneous test case with SPH (first row), MWSPH-M3 (second row) and MWSPH-M4 (third row), for $\lambda = 0.1$ (left column) and $\lambda = 0.01$ (right column), by using $200 \times 200$ initially uniformly distributed. In all cases $\sigma = 3.0$, $\sigma_{mls} = 4.5$, $CFL = 0.9$ and $\beta = \pi/6$. Negative concentrations are indicated in gray.

### 4.2. Numerical diffusion and its impact on quantifying dilution

Following Boso et al. [9], we use the dilution index [37] and the scalar dissipation rate [8] to quantify the accuracy of the proposed numerical methods in reproducing solute dilution. According to Kitanidis [37] the dilution index is defined as:

$$E(t) = \exp\left(-\sum_{k=1}^{N} P_k \ln P_k\right), \tag{30}$$

where $P_k = C_k/M$, $M$ is the total solute mass and $N$ is the total number of particles. In Eq. (30) we consider only dimensionless concentrations larger than $10^{-16}$ in order to avoid negative concentration values in the argument of the logarithm. As clearly shown by Kitanidis [37] the dilution index grows with the volume of the plume and therefore it can be used as a global indicator of numerical diffusion, which acts by increasing the volume of water occupied by the solute beyond the effect of local dispersion. The correct estimation of the dilution index is of particular relevance for the investigation of mixing processes in aquifers (e.g., [53]) and it can be informative for the estimation of the length of contaminant plumes [12,47].

Another important global quantity is the scalar dissipation rate $\chi$, which assumes the following expression:

$$\chi(t) = \int_{\Omega} \nabla C \cdot \mathbf{D} \cdot \nabla C d\Omega, \tag{31}$$

where $\Omega$ is the volume of the computational domain. The scalar dissipation rate $\chi(t)$ quantifies the rate of dissipation of concentration fluctuations by means of local dispersion and enters into the computation of global reaction kinetics for mixing-controlled precipitation-dissolution reactions [18]. Considering that both SPH and MWSPH provide a discretized representation of the concentration distribution at the particles positions, Eq. (31), can be approximated as follows:

$$\chi(t) = \sum_{i=1}^{N} V_i \nabla C_i \cdot \mathbf{D}_i \cdot \nabla C_i, \tag{32}$$

where the volume $V_i$ of the $i$th particle changes as it moves along the streamline.The scalar dissipation rate computed through (32) is a good metric to quantify numerical diffusion, mainly because it is sensitive to errors in the computation of the concentration gradient [8].

Fig. 6(a) and (b) shows the dilution index $E$ for anisotropy ratio $\lambda$ set equal to 0.1 and 0.01, respectively, obtained by substituting into Eq. (30) the concentrations computed at the particle nodes by the three numerical schemes and the analytical solution (28). In all cases the same grid of $N = 40,401$ nodes is used and except for the additional value of $\lambda$ the parameters are the same used in the test case described in Section 4.1 and reported in Table 1. The dilution index obtained with the analytical solution of the concentration (solid black line in Fig. 6) is therefore the benchmark against which the numerical schemes are compared. Notice that

the dilution index is a global quantity, which complements the analysis performed in Section 4.1. Inspection of the figures, reveals that the best match with the analytical solution is obtained by the standard SPH, with MWSPH-M3 slightly overestimating and MWSPH-M4 underestimating the dilution index. The insensitivity of the two MWSPH schemes to particle distribution, already evidenced in Section 4.1 is confirmed here (blue and green dashed lines cannot be distinguished from the corresponding solid lines), while standard SPH results in smaller $E$ values when applied with irregularly distributed particles. The good performance of SPH in terms of dilution index can be explained as a compensating effect of overestimation of large concentrations and underestimation of small concentration. Notice that negative concentrations of relatively large magnitude are distributed over larger portions of the computational domain when SPH is used (see Fig. 8). This is a significant limitation for the computation of the dilution index, which require the computation of the logarithm of solute concentration.

The maximum magnitude of negative concentrations is shown in Fig. 7 as a function of time for the three numerical schemes. Given that the concentrations are dimensionless with respect to $M/(w^2 b)$, the magnitude of the concentration is bounded between 0 and 1, in the absence of numerical errors.

Both MWSPH schemes produce fewer negative concentrations with the maximum absolute value that stabilizes after an initial rapid growth to a value, which is orders of magnitude smaller than with SPH (Fig. 7). The influence of the degree of anisotropy on negative concentrations is hardly detectable with MWSPH, but significant with SPH, whose maximum absolute value increases with

the anisotropic ratio. In agreement with what already evidenced in the discussion of Figs. 5a and 5(b) the choice of the smoothing length has a more pronounced effect on standard SPH than MWSPH. Fig. 8(a)–(f) shows the spatial distribution of the dimensionless concentrations at the dimensionless time $t = 10$, obtained with the three numerical schemes for an anisotropy $\lambda$ ratio set equal to 0.1 (left column) and 0.01 (right column). Negative concentrations are shown in gray. Curvilinear bands of negative concentration are observed in all plots, but their extension changes with the adopted numerical scheme and the anisotropy ratio. In general the area with negative concentrations is larger for $\lambda = 0.01$ than for $\lambda = 0.1$. However, the most important result shown in these figures is that SPH leads to a much wider area with negative concentrations than MWSPH. Consequently, SPH is more affected by the occurrence of negative concentrations than MWSPH. This compensation effect is small to negligible for MWSPH-M3, which underestimates slightly concentrations around the peak, thereby leading to a slight overestimation of $E$. MWSPH-M4 is much closer to the analytical solution because of an overall better approximation of the concentrations across the plume.

A metric of dilution that is free of compensating effects, because of its quadratic form, is the dissipation rate (31). Fig. 9 shows the dissipation rate, obtained using the expression equation (32) for all cases considered in the present work. Both MWSPH schemes reproduce accurately the dissipation rate $\chi$ at all times (similarly to the dilution index the benchmark is the expression of $\chi$ obtained by substituting into Eq. (32) the concentration gradients computed from the analytical solution (28)). The accuracy deteriorates



(a) *standard SPH, anisotropic ratio* $\lambda = 0.1$

(b) *standard SPH, anisotropic ratio* $\lambda = 0.01$

(c) *MWSPH M=4, anisotropic ratio* $\lambda = 0.1$

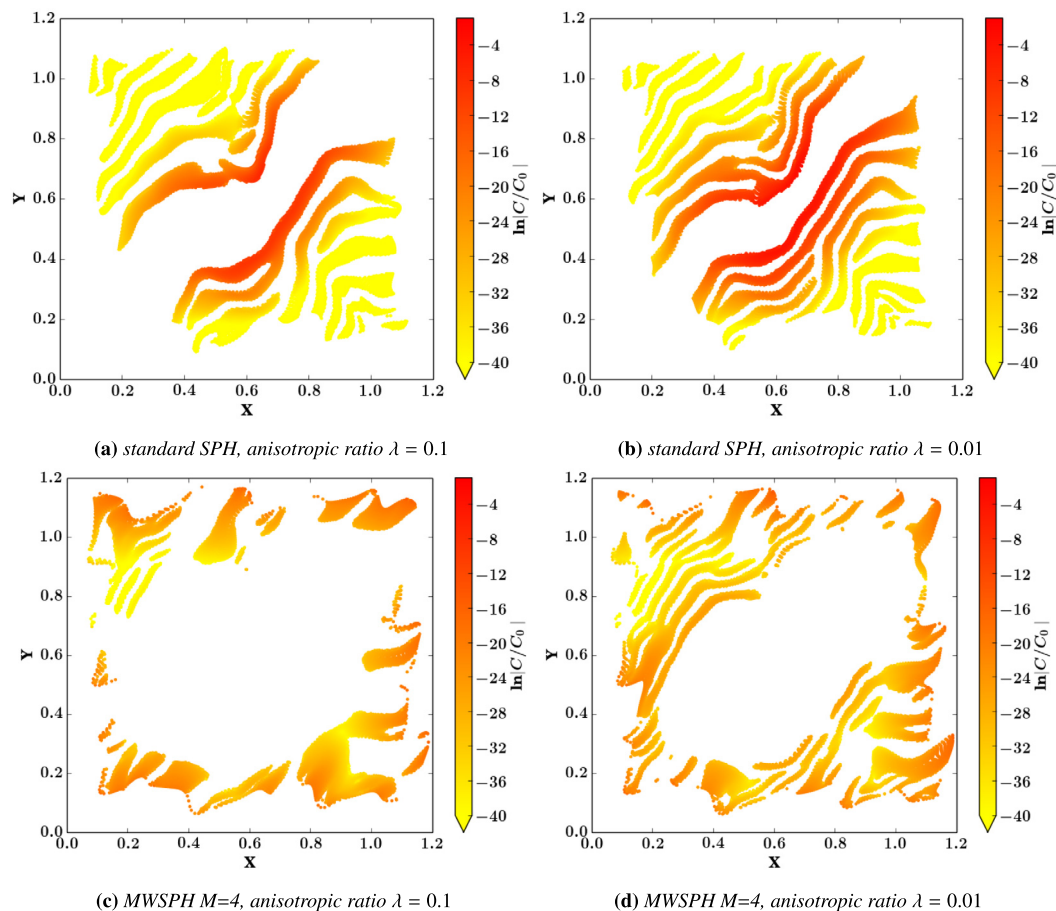(d) *MWSPH M=4, anisotropic ratio* $\lambda = 0.01$

**Fig. 14.** Negative concentration distribution for the heterogeneous test case at dimensionless time $t = 12$. Computations are performed by using SPH, MWSPH-M3 and MWSPH-M4, with $\sigma = 3.0$, $\sigma_{mls} = 4.5$ and $CFL = 0.9$.
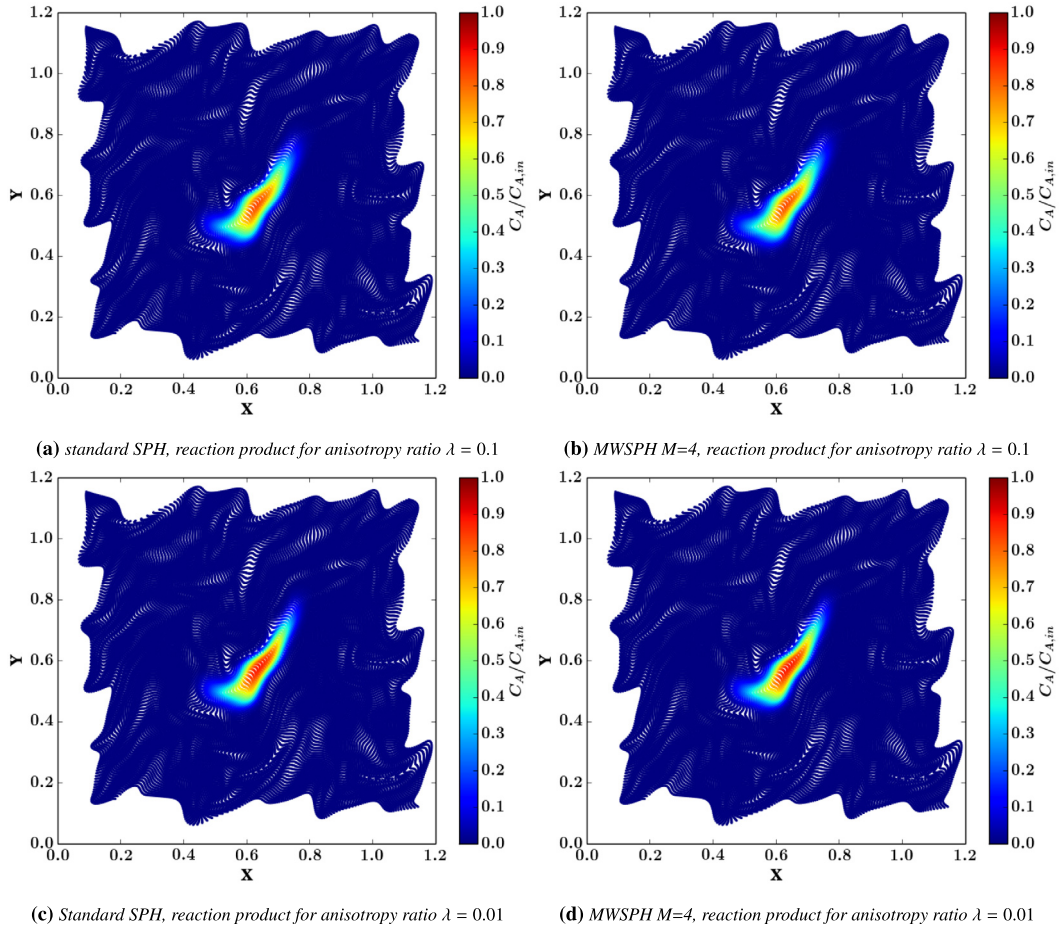
**(a)** *standard SPH, reaction product for anisotropy ratio* $\lambda = 0.1$

**(b)** *MWSPH M=4, reaction product for anisotropy ratio* $\lambda = 0.1$

**(c)** *Standard SPH, reaction product for anisotropy ratio* $\lambda = 0.01$

**(d)** *MWSPH M=4, reaction product for anisotropy ratio* $\lambda = 0.01$

**Fig. 15.** Spatial distribution of the concentration of the species A, computed with the mixing ratio $X$ obtained by solving the transport equation with SPH, MWSPH-M3 and MWSPH-M4, respectively. In all cases, $\sigma = 3.0$, $\sigma_{mls} = 4.5$ and $CFL = 0.9$.

significantly when concentration gradients are computed by SPH, as clearly shown in Fig. 9. Also for this metric, SPH is sensitive to the spatial distribution of the particles, while MWSPH is not.

### 4.3. Convergence and computational cost

The considerable gain in terms of accuracy of the MWSPH method is associated with an increase of the computational cost. Here we analyze the convergence of the numerical schemes and evaluate their computational cost. Convergence is evaluated by computing the following norms of the error evaluated as the difference at the computational nodes (particles) of the numerical and analytical solutions:

$$\epsilon_{L_p} = \sqrt[p]{\sum_i^N |C_i - C(x_i, y_i, t)|^p / N} \tag{33}$$

where the analytical solution $C(x_i, y_i, t)$ is provided by Eq. (28), $p \in [1, 2] \cup p \in \mathbf{N}$ and $\epsilon_{L_\infty} = max(|C_i - C(x_i, y_i, t|)$.

Table 2 summarizes the results of the convergence test obtained starting with a grid spacing of $\Delta x = 0.02$ and reducing it by a factor of 2 at each successive step. The values of the norms for the selected $\Delta x$ are reported in Table 2, while Fig. 10 shows $L_1$ as a function of $1/\Delta x$. The convergence rate of MWSPH is larger than for SPH, though with a relatively coarse grid spacing MWSPH-M3 shows larger $L_1$ and $L_2$ norms, while $L_\infty$ is the same. The rate of convergence of MWSPH-M3 is slightly smaller than that of MWSPH-

M4 at relatively large particle spacing (i.e. small values of $1/\Delta x$), but becomes larger as the spacing reduces, leading to nearly the same $L_1$-norm at the smallest investigated spacing of $\Delta x = 0.25 \cdot 10^{-2}$ (see Fig. 10). This is in agreement with the general property of polynomial interpolation: the order of the polynomial becomes progressively immaterial as the spacing is reduced. However, the observed reduction of the convergence rate with the reduction of the spacing (i.e. the increase of the number of particles) is dramatic below $\Delta x = 0.005$ for SPH and much less evident for MWSPH, demonstrating that though no appreciable gain is obtained by increasing the order of polynomial reconstruction, the combined action of WENO and polynomial reconstruction is extremely beneficial for the accuracy of the numerical scheme. The price to pay for this gain in accuracy, which shows an almost quadratic convergence rate at small spacing, is a larger computational burden.

The CPU time for particles distributed uniformly within the domain is reported in Table 2 for an Intel(R) Core(TM) i7-2640M CPU 2.80 GHz single processor. As expected, MWSPH is much more demanding in terms of CPU time than SPH (up to two orders of magnitude), because of the computationally expensive MLS-WENO reconstruction and stencils construction. The payoff for this larger computational effort is the higher convergence rate. Fig. 11 shows the $L_1$-norm as a function of the CPU time. While SPH is less expensive than MWSPH for relatively low, yet acceptable in many applications, accuracy (i.e., for $L_1 > 2 \cdot 10^{-5}$), the situation reverses when high accuracy is required, because of its larger rate of

convergence. Notice that the CPU time in Table 2 should be considered in relative terms, since the running time can be drastically reduced by parallelization of the code.

## 5. Conservative transport in a heterogeneous flow field

In this Section we compare the accuracy of MWSPH-M4 against SPH in modeling transport in a heterogeneous flow field. We focus on MWSPH-M4, which provides the best compromise between computational cost and accuracy of the numerical solution. To eliminate the effects of the errors introduced by the numerical solution of the flow equation, we consider the following analytical dimensionless flow field:

$$v_x(x,y) = 1 + \sum_{k=1}^{m} A_k n_{yk} \pi \cos\left(n_{xk}\pi x - \frac{\pi}{2}\right)\cos\left(n_{yk}\pi y\right), \quad (34a)$$

$$v_y(x,y) = 1 + \sum_{k=1}^{m} A_k n_{yk} \pi \sin\left(n_{xk}\pi x - \frac{\pi}{2}\right)\sin\left(n_{yk}\pi y\right), \quad (34b)$$

which has been proposed by Nakshatrala et al. [43]. In Eq. (34) the velocity is dimensionless with respect to a given mean velocity $|\mathbf{v}|$ and lengths are dimensionless with respect to the wavelength $L$ of the velocity fluctuations. Furthermore, $m$ is the number of harmonics, which we set equal to 3, and the other quantities are: $(n_{x1}, n_{x2}, n_{x3}) = (4, 5, 10)$, $(n_{y1}, n_{y2}, n_{y3}) = (1, 5, 10)$, $(A_1, A_2, A_3) = (8, 2, 1)$. Fig. 12(a) shows the resulting heterogeneous velocity field and Fig. 12(b) depicts the initial condition: an instantaneous

injection of a nonreactive tracer in a square of size $S_x = S_y = 30$ centered at $(x = 35/81, y = 35/81)$ and unitary initial dimensionless concentration. The local dispersion tensor is anisotropic with a constant longitudinal Peclèt number $Pe = L/\alpha_L = 100$ and ratio of anisotropy $\lambda = \alpha_T/\alpha_L$, where $\alpha_L$ and $\alpha_T$ are the longitudinal and transverse dispersivities, respectively. Particles are initially placed at the nodes of a regular square lattice. Finally, time is dimensionless with respect to the characteristic advection time: $T = L/|\mathbf{v}|$.

Fig. 13 shows the spatial distribution of the concentration at the dimensionless time $T = 10$ since the injection, obtained by applying SPH and MWSPH with the above velocity field and for both $\lambda = 0.1$ (left column) and $\lambda = 0.01$ (right column). Spurious negative concentrations are marked in gray. Similarly to the homogeneous case, when MWSPH is used negative concentrations are distributed over a smaller area and are at a larger distance from the main plume body than with SPH. This difference is more pronounced for high anisotropy, i.e. small $\lambda$, as can be seen by comparing the two columns in Fig. 13. The better performance of MWSPH is due to a more accurate reproduction of local concentration gradients, which leads to a better estimation of spatially variable concentration fluxes even when particles are non-uniformly distributed within the computational domain, due to the heterogeneity of the velocity field. This is a property of the solver that is particularly appreciated when high accuracy is required in the reproduction of local concentration fluxes, such as in modeling transport of species reacting upon mixing, for example. The color plots of Fig. 14(a) and (b) shows the spatial distribution of the absolute value of the negative concentration for SPH and
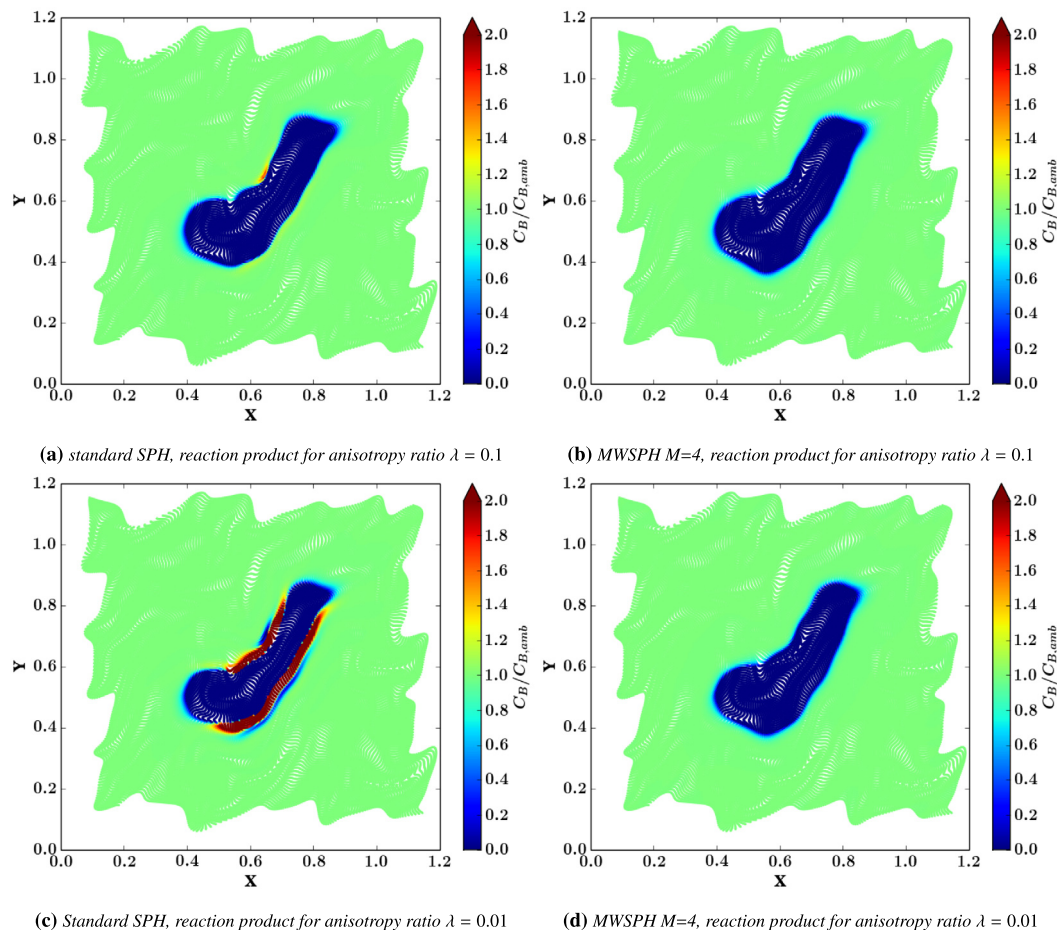


(a) *standard SPH, reaction product for anisotropy ratio* $\lambda = 0.1$

(b) *MWSPH M=4, reaction product for anisotropy ratio* $\lambda = 0.1$

(c) *Standard SPH, reaction product for anisotropy ratio* $\lambda = 0.01$

(d) *MWSPH M=4, reaction product for anisotropy ratio* $\lambda = 0.01$

**Fig. 16.** Spatial distribution of the concentration of the species B, computed with the mixing ratio $X$ obtained by solving the transport equation with SPH, MWSPH-M3 and MWSPH-M4, respectively. In all cases $\sigma = 3.0$, $\sigma_{mls} = 4.5$ and $CFL = 0.9$.
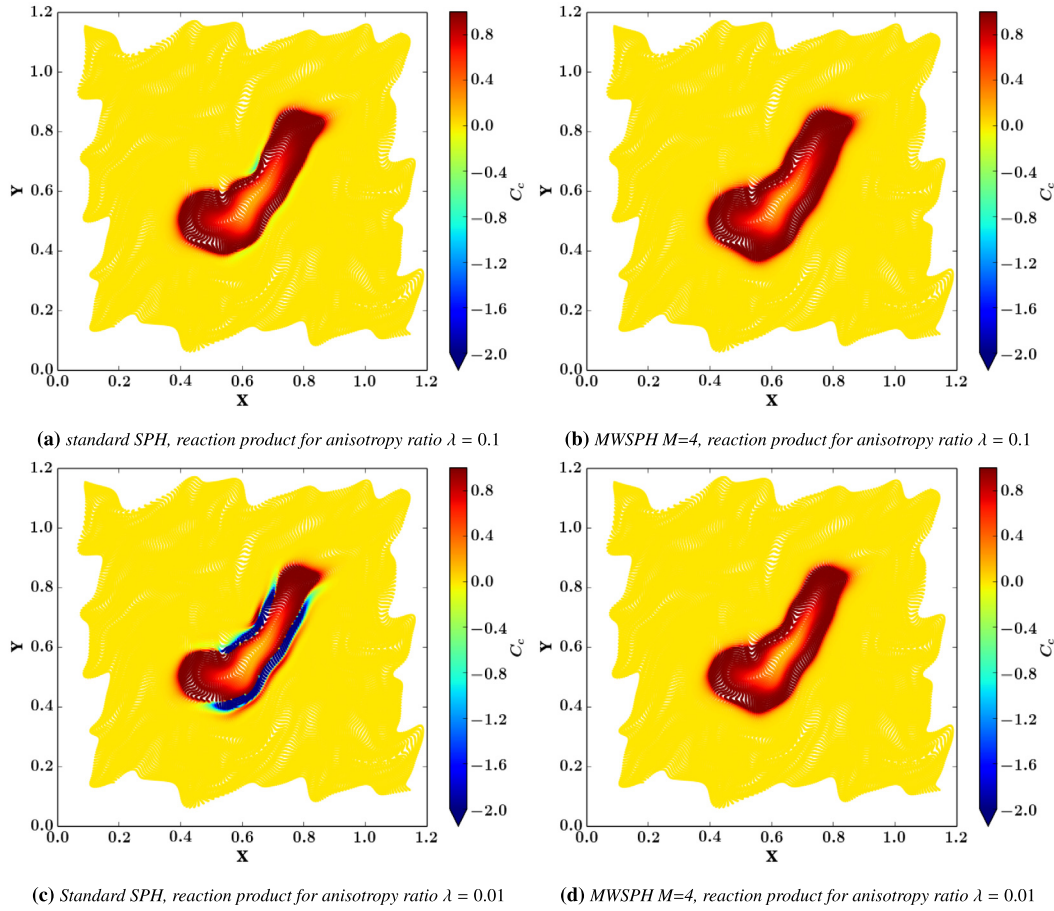
**(a)** *standard SPH, reaction product for anisotropy ratio $\lambda = 0.1$*

**(b)** *MWSPH M=4, reaction product for anisotropy ratio $\lambda = 0.1$*

**(c)** *Standard SPH, reaction product for anisotropy ratio $\lambda = 0.01$*

**(d)** *MWSPH M=4, reaction product for anisotropy ratio $\lambda = 0.01$*

**Fig. 17.** Spatial distribution of the concentration of the product C, computed with the mixing ratio $X$ obtained by solving the transport equation with SPH, MWSPH-M3 and MWSPH-M4, respectively. In all cases $\sigma = 3.0$, $\sigma_{mls} = 4.5$ and $CFL = 0.9$.

MWSPH. Negative concentrations occupy a much smaller area and are of much smaller absolute value (notice the logarithmic color scale) when transport is simulated using MWSPH, thus confirming also visually the better performance of MWSPH in modeling transport in heterogeneous velocity fields. The solute concentration computed according to the standard SPH scheme leads to negative concentrations of the order of $10^{-3}$ and $10^{-2}$, for $\lambda = 0.1$ and $\lambda = 0.01$, respectively, while the MWSPH scheme reduces this error by four orders of magnitude down to $10^{-7}$ and $10^{-6}$, respectively, which can be considered a significant improvement.

The occurrence of spurious oscillations and of negative concentrations is particularly problematic when dealing with reactive transport under mixing controlled conditions. A representative case of two-species solute transport, useful for illustrative purposes, is the following instantaneous irreversible bimolecular reaction between species $A$ and $B$, which produces the species $C$ according to the following stoichiometry: $f_A A + f_B B \rightarrow f_C C$, where $f_A$, $f_B$ and $f_C$ are the stoichiometric coefficients of the reaction. This reaction has been used by Kapoor et al. [34] to study the effect of flow heterogeneity on bimolecular reactions and later in studies dealing with the effect of heterogeneity on mixing (see e.g., [19,20,57]). Under the hypothesis that the two reacting species share the same molecular diffusion coefficient (see [11] for an in depth discussion on this point), the following relationship can be established between the concentrations of the three species ($C_A$, $C_B$ and $C_C$) and the reaction ratio $X$, which is a normalized variable bounded between 0 and 1:

$$
\left.\begin{aligned}
C_A &= X \cdot C_{A,in} - (1-X)\frac{f_A}{f_B} \cdot C_{B,amb} \\
C_B &= 0 \\
C_C &= (1-X)\frac{f_C}{f_B} \cdot C_{B,amb}
\end{aligned}\right\} \text{ for } X > X_{crit};
\tag{35}
$$

$$
\left.\begin{aligned}
C_A &= 0 \\
C_B &= (1-X) \cdot C_{B,amb} - X\frac{f_B}{f_A} \cdot C_{A,in} \\
C_C &= X \cdot \frac{f_C}{f_A} A_{in}
\end{aligned}\right\} \text{ for } X \leqslant X_{crit},
\tag{36}
$$

where $X_{crit}$ is defined as follows:

$$
X_{crit} = \frac{f_A C_{B,amb}}{f_B C_{A,in} + f_A C_{B,amb}};
\tag{37}
$$

where $C_{A,in}$ is the concentration of the species $A$ in the injected water and $C_{B,amb}$ is the concentration of the species $B$ in the ambient water. In this context, the mixing ratio represents the fraction of source water in the ambient water and is a conservative quantity satisfying the ADE. This property simplifies the mathematical problem, which reduces to the solution of the ADE for the mixing ratio $X$ with suitable initial and boundary conditions, followed by the substitution of $X$ into the stoichiometric equations (35) and (36) to obtain the concentration of the single species. As shown in Fig. 15 the concentration of the species $A$ is insensitive to the numerical scheme adopted, simply because according to Eq. (36) $C_A$ is set to zero for low $X$ values (i.e., $X < X_{crit}$), thereby the error introduced by the numerical scheme at low concentrations of $X$ is immaterial in the computation of the concentration of this reactant. The

influence of the numerical scheme is instead clearly visible in the spatial distribution of the reactant $B$ and the product $C$. Numerical simulations have been performed with the following parameters: $C_{A,in} = 1$, $C_{B,amb} = 0.001$ (dimensionless with reference to a given concentration), $f_A = 1$, $f_B = 1$ and $f_C = 1$. Numerical artifacts introduced by SPH are clearly visible in the Figs. 16 and 17, showing the concentration distribution of the reactant $B$ and the product $C$, respectively. Areas of negative concentrations of the product appear at the plume fringes, whose extension is larger for larger anisotropy. Notice that the occurrence of negative product concentrations corresponds to regions in which the mixing ratio is negative. In the same regions, the reaction partner $B$ is generated instead of consumed during the reaction, as shown in Fig. 16. These unphysical results are absent in the MWSPH-M4 simulations.

## 6. Conclusion

We have derived a new SPH formulation based on a high-order non-linear Moving-Least-Squares WENO reconstruction on moving point clouds.The comparison with the classic SPH scheme has shown the advantages offered by the novel scheme in term of accuracy achieved in simulating transport of conservative and reactive solutes in homogeneous and heterogeneous porous media. In particular, MWSPH is very effective in limiting the occurrence of negative concentrations and spurious oscillations and the accuracy of the numerical solution does not deteriorate at higher anisotropy of the local dispersion tensor. This accommodates for one of the main drawbacks of SPH, which generates increasingly negative concentrations as the anisotropy in the dispersion is more relevant. As expected, the accuracy of the MWSPH scheme depends on the order of the reconstructed polynomial. In addition, convergence analysis shows that the MWSPH is more accurate than the standard SPH scheme and shows a much larger convergence rate. Negative concentrations of the order of $10^{-2} - 10^{-3} C_0$, where $C_0$ is the initial concentration, are observed with SPH, while MWSPH limits the absolute value of negative concentrations to about $10^{-7} C_0$.

Avoiding the occurrence of unphysical negative concentrations is important in all cases where high accuracy is required, such as in multi-species mixing-controlled reactive solute transport. The proposed MWSPH scheme can be also applied to transient flow fields. This is an important advantage of MWSPH because most of the improvements to the SPH scheme are limited to steady state flows when an anisotropic dispersion tensor is considered [32].

## References

[1] Agossler Albert A. Moving least-squares: a numerical differentiation method for irregularly spaced calculation points. Technical report, Sandia National Labs; 2001.

[2] Arbogast T, Huang C. A fully mass and volume conserving implementation of a characteristic method for transport problems. SIAM J Sci Comput 2006;28(6):2001–22. http://dx.doi.org/10.1137/040621077.

[3] Arbogast T, Huang C, Hung C. A fully conservative Eulerian–Lagrangian streamtube method for advection–diffusion problems. SIAM J Sci Comput 2012;34(4):B447–78. http://dx.doi.org/10.1137/110840376.

[4] Arbogast T, Huang C, Russell T. A locally conservative Eulerian–Lagrangian method for a model two-phase flow problem in a one-dimensional porous medium. SIAM J Sci Comput 2012;34(4):A1950–74. http://dx.doi.org/10.1137/090778079.

[5] Arbogast T, Huang C-S. A fully conservative Eulerian–Lagrangian method for a convection–diffusion problem in a solenoidal field. J Comput Phys 2010;229(9):3415–27. http://dx.doi.org/10.1016/j.jcp.2010.01.009.

[6] Avesani D, Dumbser M, Bellin A. A new class of moving-least-squares weno-sph schemes. Journal of Computational Physics 2014;270:278–99. http://dx.doi.org/10.1016/j.jcp.2014.03.041.

[7] Bear J. Dynamics of Fluids in Porous Media. Dover Books on Physics & Chemistry. Dover Publ; 1972. http://books.google.cl/books?id=lurrmlFGhTEC.

[8] Borgne TL, Dentz M, Bolster D, Carrera J, de Dreuzy J-R, Davy P. Non-fickian mixing: Temporal evolution of the scalar dissipation rate in heterogeneous porous media. Advances in Water Resources 2010;33(12):1468–75. http://dx.doi.org/10.1016/j.advwatres.2010.08.006.

[9] Boso F, Bellin A, Dumbser M. Numerical simulations of solute transport in highly heterogeneous formations: A comparison of alternative numerical schemes. Advances in Water Resources 2013;52:178–89. http://dx.doi.org/10.1016/j.advwatres.2012.08.006. http://www.sciencedirect.com/science/article/pii/S0309170812002266.

[10] Brookshaw L. A method of calculating radiative heat diffusion in particle simulations. Astronomical Society of Australia 1985;6(2):207–10.

[11] Chiogna G, Cirpka OA, Grathwohl P, Rolle M. Relevance of local compound-specific transverse dispersion for conservative and reactive mixing in heterogeneous porous media. Water Resources Research 2011;47(7). http://dx.doi.org/10.1029/2010WR010270. n/a–n/a.

[12] Chiogna G, Cirpka OA, Grathwohl P, Rolle M. Transverse mixing of conservative and reactive tracers in porous media: Quantification through the concepts of flux-related and critical dilution indices. Water Resources Research 2011;47(2).

[13] Chiogna G, Hochstetler DL, Bellin A, Kitanidis PK, Rolle M. Mixing, entropy and reactive solute transport. Geophysical Research Letters 2012;39(20). http://dx.doi.org/10.1029/2012GL053295. n/a–n/a.

[14] Cirpka OA, Frind EO, Helmig R. Numerical methods for reactive transport on rectangular and streamline-oriented grids. Advances in Water Resources 1999;22(7):711–28. http://dx.doi.org/10.1016/S0309-1708(98)00051-7.

[15] Cirpka OA, Valocchi AJ. Two-dimensional concentration distribution for mixing-controlled bioreactive transport in steady state. Adv Water Resour 2007;30(6–7):1668–79 (Biological processes in porous media: From the pore scale to the field). http://dx.doi.org/10.1016/j.advwatres.2006.05.022.

[16] Cleary PW, Monaghan JJ. Conduction modelling using smoothed particle hydrodynamics. Journal of Computational Physics 1999;148(1):227–64. http://dx.doi.org/10.1006/jcph.1998.6118. http://www.sciencedirect.com/science/article/pii/S0021999198961186.

[17] Courant R, Friedrichs K, Lewy H. +?ber die partiellen differenzengleichungen der mathematischen physik. Mathematische Annalen 1928;100(1):32–74. http://dx.doi.org/10.1007/BF01448839.

[18] De Simoni M, Carrera J, Sanchez-Vila X, Guadagnini A. A procedure for the solution of multicomponent reactive transport problems. Water Resources Research 2005;41(11). http://dx.doi.org/10.1029/2005WR004056. n/a–n/a.

[19] Ding D, Benson DA, Paster A, Bolster D. Modeling bimolecular reactions and transport in porous media via particle tracking. Advances in Water Resources 2013;53:56–65. http://dx.doi.org/10.1016/j.advwatres.2012.11.001. http://www.sciencedirect.com/science/article/pii/S030917081200276X.

[20] Donado LD, Sanchez-Vila X, Dentz M, Carrera J, Bolster D. Multicomponent reactive transport in multicontinuum media. Water Resources Research 2009;45(11). http://dx.doi.org/10.1029/2008WR006823. n/a–n/a.

[21] Dumbser M. Arbitrary high order PNPM schemes on unstructured meshes for the compressible Navier-Stokes equations. Computers & Fluids 2010;39(1):60–76. http://dx.doi.org/10.1016/j.compfluid.2009.07.003.

[22] Dumbser M, Käser M. Arbitrary high order non-oscillatory finite volume schemes on unstructured meshes for linear hyperbolic systems. Journal of Computational Physics 2007;221(2):693–723. http://dx.doi.org/10.1016/j.jcp.2006.06.043. http://www.sciencedirect.com/science/article/pii/S0021999106003123.

[23] Dumbser M, Käser M, Titarev VA, Toro EF. Quadrature-free non-oscillatory finite volume schemes on unstructured meshes for nonlinear hyperbolic systems. Journal of Computational Physics 2007;226(1):204–43. http://dx.doi.org/10.1016/j.jcp.2007.04.004. http://www.sciencedirect.com/science/article/pii/S0021999107001520.

[24] Espanol P, Revenga M. Smoothed dissipative particle dynamics. Phys. Rev. E 2003;67:026705. http://dx.doi.org/10.1103/PhysRevE.67.026705. http://link.aps.org/doi/10.1103/PhysRevE.67.026705.

[25] Ferrari A, Dumbser M, Toro EF, Armanini A. A new 3d parallel sph scheme for free surface flows. Computers & Fluids 2009;38(6):1203–17. http://dx.doi.org/10.1016/j.compfluid.2008.11.012. http://www.sciencedirect.com/science/article/pii/S0045793008002284.

[26] Gassner G, Lörcher F, Munz C-D. A contribution to the construction of diffusion fluxes for finite volume and discontinuous galerkin schemes. Journal of Computational Physics 2007;224(2):1049–63. http://dx.doi.org/10.1016/j.jcp.2006.11.004. http://www.sciencedirect.com/science/article/pii/S0021999106005651.

[27] Gingold RA, Monaghan JJ. Smoothed particle hydrodynamics - Theory and application to non-spherical stars. Mon. Not. Roy. Astron. Soc. 1977;181:375–89. http://adsabs.harvard.edu/cgi-bin/nph-bib_query?bibcode=1977MNRAS.181..375G.

[28] Gottlieb S, wang Shu C. Total variation diminishing runge-kutta schemes. Math. Comp 1998;67:73–85.

[29] Herrera, P. (2009). Particle and streamline numerical methods for conservative and reactive transport simulations in porous media. PhD thesis, University of British Columbia.

[30] Herrera PA, Beckie RD. An assessment of particle methods for approximating anisotropic dispersion. International Journal for Numerical Methods in Fluids 2013;71(5):634–51. http://dx.doi.org/10.1002/fld.3676.

[31] Herrera PA, Massab M, Beckie RD. A meshless method to simulate solute transport in heterogeneous porous media. Advances in Water Resources 2009;32(3):413–29. http://dx.doi.org/10.1016/j.advwatres.2008.12.005. http://www.sciencedirect.com/science/article/pii/S0309170808002273.

[32] Herrera PA, Valocchi AJ, Beckie RD. A multidimensional streamline-based method to simulate reactive solute transport in heterogeneous porous media. Advances in Water Resources 2010;33(7):711–27. http://dx.doi.org/10.1016/j.advwatres.2010.03.001. http://www.sciencedirect.com/science/article/pii/S0309170810000424.

[33] Hidalgo A, Dumbser M. ADER schemes for nonlinear systems of stiff advection-diffusion-reaction equations. Journal of Scientific Computing 2011;48:173–89. http://dx.doi.org/10.1007/s10915-010-9426-6.

[34] Kapoor V, Gelhar LW, Miralles-Wilhelm F. Bimolecular second-order reactions in spatially varying flows: Segregation induced scale-dependent transformation rates. Water Resour. Res. 1997;33(4):527–36.

[35] Kim M-Y, Wheeler MF. Coupling discontinuous galerkin discretizations using mortar finite elements for advection-diffusion-reaction problems. Computers & Mathematics with Applications 2014;67(1):181–98. http://dx.doi.org/10.1016/j.camwa.2013.11.002. http://www.sciencedirect.com/science/article/pii/S0898122113006561.

[36] Kim M-Y, Wheeler MF. A multiscale discontinuous Galerkin method for convection–diffusion–reaction problems. Comput Math Appl 2014;68(12, Part B):2251–61 (Advances in computational partial differential equations). http://dx.doi.org/10.1016/j.camwa.2014.08.007. http://www.sciencedirect.com/science/article/pii/S0898122114003678.

[37] Kitanidis PK. The concept of dilux index. Water Resources Research 1994;30(7):2011–26.

[38] Liu Y, Illangasekare TH, Kitanidis PK. Long-term mass transfer and mixing-controlled reactions of a {DNAPL} plume from persistent residuals. Journal of Contaminant Hydrology 2014;157:11–24. http://dx.doi.org/10.1016/j.jconhyd.2013.10.008. http://www.sciencedirect.com/science/article/pii/S0169772213001563.

[39] Long W, Hilpert M. Analytical solutions for bacterial energy taxis (chemotaxis): Traveling bacterial bands. Advances in Water Resources 2007;30(11):2262–70. http://dx.doi.org/10.1016/j.advwatres.2007.05.007. http://www.sciencedirect.com/science/article/pii/S0309170807000838.

[40] Lucy LB. A numerical approach to the testing of the fission hypothesis. Astronomical Journal 1977;82:1013–24. http://dx.doi.org/10.1086/112164.

[41] Monaghan JJ. Simulating free surface flows with sph. Journal of Computational Physics 1994;110:399–406. http://dx.doi.org/10.1006/jcph.1994.1034. http://adsabs.harvard.edu/abs/1994JCoPh.110..399M.

[42] Monaghan JJ. Smoothed particle hydrodynamics. Reports on Progress in Physics 2005;68(8):1703. http://stacks.iop.org/0034-4885/68/i=8/a=R01.

[43] Nakshatrala KB, Mudunuru MK, Valocchi AJ. A numerical framework for diffusion-controlled bimolecular-reactive systems to enforce maximum principles and the non-negative constraint. J Comput Phys 2013;253:278–307. http://dx.doi.org/10.1016/j.jcp.2013.07.010.

[44] Obi E-O, Blunt MJ. Streamline-based simulation of advective dispersive solute transport. Advances in Water Resources 2004;27(9):913–24. http://dx.doi.org/10.1016/j.advwatres.2004.06.003. http://www.sciencedirect.com/science/article/pii/S0309170804000983.

[45] Pan W, Bao J, Tartakovsky AM. Smoothed particle hydrodynamics continuous boundary force method for navier-stokes equations subject to a robin boundary condition. Journal of Computational Physics 2014;259:242–59. http://dx.doi.org/10.1016/j.jcp.2013.12.014. http://www.sciencedirect.com/science/article/pii/S0021999113008139.

[46] Paster A, Bolster D, Benson DA. Particle tracking and the diffusion-reaction equation. Water Resources Research 2013;49(1):1–6. http://dx.doi.org/10.1029/2012WR012444.

[47] Rolle M, Eberhardt C, Chiogna G, Cirpka OA, Grathwohl P. Enhancement of dilution and transverse reactive mixing in porous media: Experiments and model-based interpretation. Journal of Contaminant Hydrology 2009;110(34)::130–142. http://dx.doi.org/10.1016/j.jconhyd.2009.10.003. http://www.sciencedirect.com/science/article/pii/S0169772209001429.

[48] Salamon P, Fernàndez-Garcia D, Gómez-Herná-fndez JJ. A review and numerical assessment of the random walk particle tracking method. Journal of Contaminant Hydrology 2006;87(3–4):277–305. http://dx.doi.org/10.1016/j.jconhyd.2006.05.005. http://www.sciencedirect.com/science/article/pii/S0169772206000957.

[49] Srinivasan G, Tartakovsky D, Dentz M, Viswanathan H, Berkowitz B, Robinson B. Random walk particle tracking simulations of non-fickian transport in heterogeneous media. Journal of Computational Physics 2010;229(11):4304–14. http://dx.doi.org/10.1016/j.jcp.2010.02.014. http://www.sciencedirect.com/science/article/pii/S0021999110000872.

[50] Tartakovsky A, Meakin P. Modeling of surface tension and contact angles with smoothed particle hydrodynamics. Phys. Rev. E 2005;72:026301. http://dx.doi.org/10.1103/PhysRevE.72.026301. http://link.aps.org/doi/10.1103/PhysRevE.72.026301.

[51] Tartakovsky AM, Meakin P, Scheibe TD, West RME. Simulations of reactive transport and precipitation with smoothed particle hydrodynamics. Journal of Computational Physics 2007;222(2):654–72. http://dx.doi.org/10.1016/j.jcp.2006.08.013. http://www.sciencedirect.com/science/article/pii/S002199910600372X.

[52] Tartakovsky AM, Meakin P, Scheibe TD, Wood BD. A smoothed particle hydrodynamics model for reactive transport and mineral precipitation in porous and fractured porous media. Water Resour. Res. 2007;43(5):W05437. http://dx.doi.org/10.1029/2005WR004770.

[53] Thierrin J, Kitanidis PK. Solute dilution at the borden and cape cod groundwater tracer tests. Water Resources Research 1994;30(11):2883–90. http://dx.doi.org/10.1029/94WR01983.

[54] Tompson A. Numerical simulation of chemical migration in physically and chemically heterogeneous porous media. Water Resour. Res. 1993;29(11):3709–26. http://dx.doi.org/10.1029/93WR01526.

[55] Tonina D, Bellin A. Effects of pore-scale dispersion, degree of heterogeneity, sampling size, and source volume on the concentration moments of conservative solutes in heterogeneous formations. Advances in Water Resources 2008;31:339–54.

[56] Vaughan GL, Healy TR, Bryan KR, Sneyd AD, Gorman RM. Completeness, conservation and error in sph for fluids. International Journal for Numerical Methods in Fluids 2008;56(1):37–62. http://dx.doi.org/10.1002/fld.1530.

[57] Werth CJ, Cirpka OA, Grathwohl P. Enhanced mixing and reaction through flow focusing in heterogeneous porous media. Water Resources Research 2006;42(12). http://dx.doi.org/10.1029/2005WR004511. n/a–n/a.

[58] Zhang X, Bengough AG, Crawford JW, Young IM. A lattice BGK model for advection and anisotropic dispersion equation. Advances in Water Resources 2002;25(1):1–8. http://dx.doi.org/10.1016/S0309-1708(01)00047-1. http://www.sciencedirect.com/science/article/pii/S0309170801000471.

[59] Zwillinger D. CRC Standard Mathematical Tables and Formulae: Editor-in-chief, Daniel Zwillinger. CRC Standard Mathematical Tables and Formulae. Taylor & Francis Group; 2003. http://books.google.cl/books?id=9zXt1yFQE2UC.